

Spatial Information in a Non-retinotopic Visual Cortex

Highlights

- Turtle visual cortex (dCx) shows no clear retinotopy
- Most receptive fields cover the entire contralateral visual field but are not uniform
- Stimulus position and contrast can be decoded from small dCx neural populations
- Adaptation to repeated local stimulation is position specific in dCx

Authors

Julien Fournier, Christian M. Müller,
Ingmar Schneider, Gilles Laurent

Correspondence

gilles.laurent@brain.mpg.de

In Brief

Fournier, Mueller et al. show that visual cortex in turtles may encode positions in the visual field despite the poor spatial selectivity of its receptive fields and the absence of fine retinotopic mapping of thalamocortical projections.



Spatial Information in a Non-retinotopic Visual Cortex

Julien Fournier,^{1,2,3} Christian M. Müller,^{1,3} Ingmar Schneider,¹ and Gilles Laurent^{1,4,*}

¹Max Planck Institute for Brain Research, Department of Neural Systems, Max von Laue Str 4, 60438 Frankfurt am Main, Germany

²Present address: Cortexlab, University College London, Cruciform Building, Gower Street, London WC1E 6BT, UK

³These authors contributed equally

⁴Lead Contact

*Correspondence: gilles.laurent@brain.mpg.de

<https://doi.org/10.1016/j.neuron.2017.11.017>

SUMMARY

Turtle dorsal cortex (dCx), a three-layered cortical area of the reptilian telencephalon, receives inputs from the retina via the thalamic lateral geniculate nucleus and constitutes the first cortical stage of visual processing. The receptive fields of dCx neurons usually occupy the entire contralateral visual field. Electrophysiological recordings in awake and anesthetized animals reveal that dCx is sensitive to the spatial structure of natural images, that dCx receptive fields are not entirely uniform across space, and that adaptation to repeated stimulation is position specific. Hence, spatial information can be found both at the single-neuron and population scales. Anatomical data are consistent with the absence of a clear retinotopic mapping of thalamocortical projections. The mapping and representation of visual space in this three-layered cortex thus differ from those found in mammalian primary visual cortex. Our results support the notion that dCx performs a global, rather than local, analysis of the visual scene.

INTRODUCTION

What are the overarching principles of cortical computation and the functional advantages conferred by its modular and pluripotent design? These important questions have thus far been explored nearly exclusively in mammals (primates, carnivores, and, more recently, rodents), and mostly (though not exclusively) in primary or “early” sensory areas (V1, A1, and S1). Yet cerebral cortex, a layered structure covering the forebrain, is not a mammalian invention. It likely evolved over 300 million years ago with the amniotes, for it is found in all mammals (monotremes, marsupials, and eutherians) and in their sister group, the sauropsids, but does not exist in either fish or amphibians (Butler et al., 2011). Among the sauropsids, cortex proper can be identified clearly only in the non-avian reptiles. Reptilian cortex, a three-layered structure similar to the mammalian paleo- and archi-cortices (piriform and hippocampal, respectively), probably resembles the common ancestral cortex in stem amni-

otes. Hence, reptiles offer a good opportunity to study a relatively simple cortex, and possibly to uncover some of the structural and computational logic of its original design.

We undertook to study turtle dorsal cortex (dCx), a system that was once the focus of classical anatomical and functional studies (Hall and Ebner, 1970; Hall et al., 1977; Heller and Ulinski, 1987; Morlock, 1972; Mulligan and Ulinski, 1990; Reiner, 1991; Zhu et al., 2005). Early anatomical studies of the visual thalamocortical system suggested an unusual mapping of the retina onto dCx, such as the loss of topography along the vertical dimension of the visual field (Mulligan and Ulinski, 1990). Previous studies (Gusel'nikov et al., 1972; Mazurskaya, 1973; Mazurskaya et al., 1967) also suggested that dCx neuron visual receptive fields (RFs) cover the entire contralateral visual field with almost no spatial selectivity and that their responses adapt strongly and rapidly to repeated visual stimulation (Gusel'nikov and Pivovarov, 1978; Hayes et al., 1968; Luo et al., 2010). Electrophysiological and voltage-sensitive dye (VSD) imaging studies (Prechtl, 1994; Prechtl et al., 1997, 2000; Senseman and Robbins, 1999, 2002) reported the existence of interlocked stimulus-evoked oscillations and wave patterns, but the cellular activity underlying those macroscopic phenomena remains unknown. Thus, the nature of visual representations in turtle dCx remains to be discovered.

Our goal was to revisit these questions with a quantitative approach using large-scale recordings and classical techniques of RF mapping used to study information processing and representation in mammalian visual cortex (DeAngelis et al., 1993; Emerson et al., 1987; Fournier et al., 2014; Levy et al., 2013; Movshon et al., 1978; Rust et al., 2005; Touryan et al., 2005). Our anatomical data show that the mapping of the visual field is not a straightforward projection onto dCx; there appears to be no retinotopic map in dCx. Consistent with the anatomy, we found that the vast majority of dCx RFs cover almost entirely the contralateral visual field. Yet we show that dCx is sensitive to the spatial and temporal statistics of natural scenes. Moreover, a substantial fraction of dCx neurons exhibit some non-uniformity in their spatial response profiles, which can be used to decode the position and contrast polarity of a stimulus.

These results show that despite their generally poor spatial selectivity, dCx neurons provide information about stimulus position, both at the single-cell and population level. The structural and functional attributes underlying this selectivity appear different from those underlying the encoding of visual space in



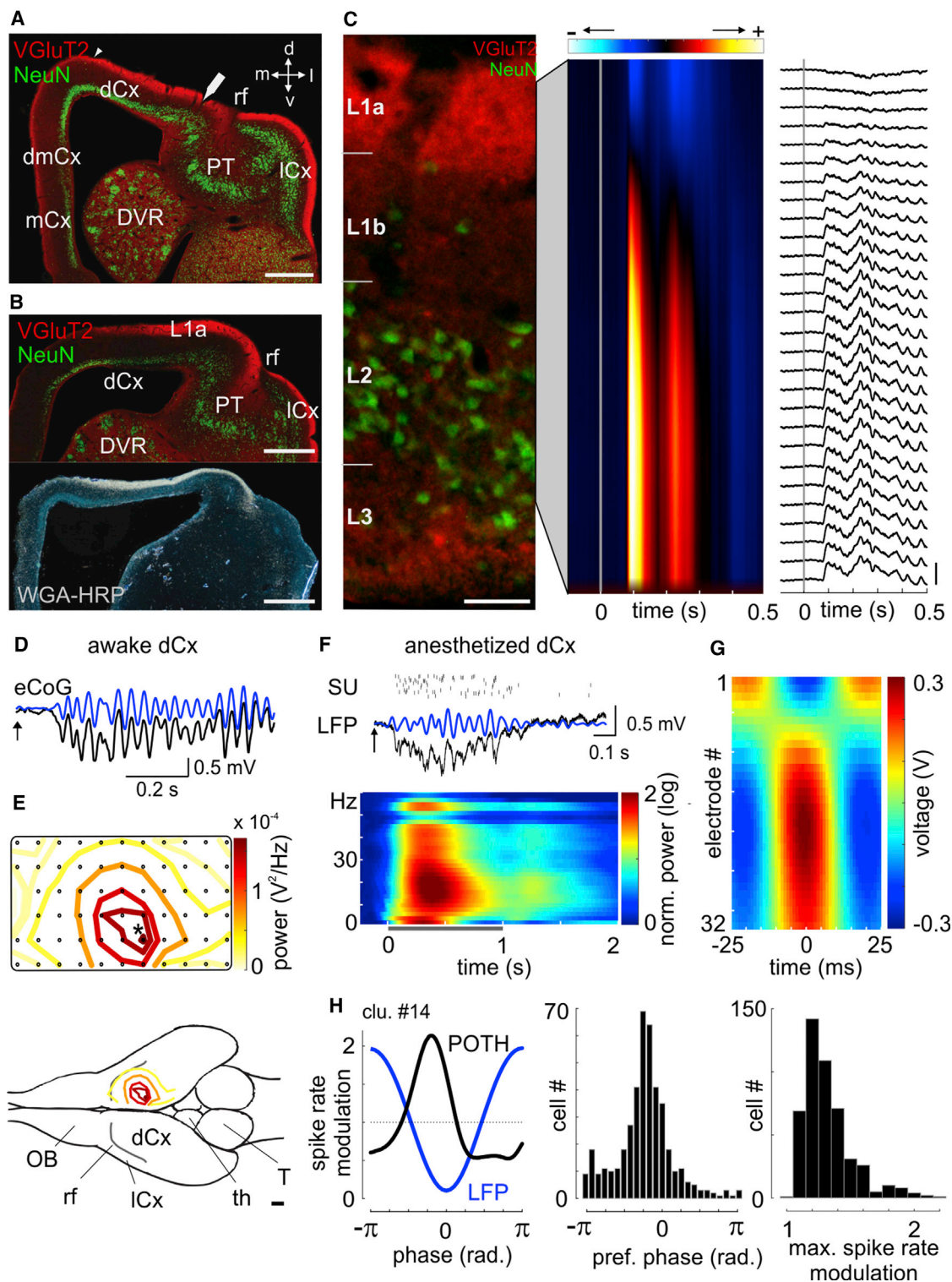


Figure 1. Histology of dCx, Mapping of Visual Responses, and Beta-Range Oscillation

(A) Frontal section stained for VGLuT2 (red), a marker of subcortical terminals, and NeuN (green), a pan-neuronal marker. dCx, dorsal cortex; rf, rhinal fissure; ICx, lateral cortex; PT, pallial thickening; dmCx, dorsomedial cortex; mCx, medial cortex; DVR, dorsal-ventricular ridge; d, dorsal; v, ventral; m, medial; l, lateral. Scale bar, 1 mm.

(B) Correlation between VGLuT2 staining (red, top) and thalamocortical LGN axon terminals revealed in layer 1a by trans-synaptic labeling after contralateral eye injection of WGA-HRP (white, bottom) (sections are from two different animals). Scale bar, 1 mm.

(legend continued on next page)

mammalian primary visual neurons (Hubel and Wiesel, 1962; Lien and Scanziani, 2013; Marshel et al., 2011). Our data argue for a distributed encoding of visual space in dCx, with no topographical mapping of the physical dimensions of the sensory space. It suggests that information processing in turtle visual cortex might rely on similar principles to those that govern object encoding in olfactory cortex and higher visual areas.

RESULTS

Functional Anatomy of dCx and Selection of Depth Recording Locations

The reptilian cortex is composed of three layers with densely packed pyramidal cells in layer 2 only, and interneurons scattered through layers 1–3 (Figure 1A). The visual dCx is traditionally divided across the latero-medial axis into two areas called D2 and D1 (Desan, 1984; Heller and Ulinski, 1987); D2 (lateral to D1) receives direct input from lateral geniculate nucleus (LGN).

Intraocular injection of the trans-synaptic tracer WGA-HRP (STAR Methods) revealed the axonal projection zone of retino-recipient LGN neurons as a densely stained superficial zone in layer 1 of dCx (L1a; Figure 1B). This projection zone was also stained by an antibody against VGluT2, a marker of subcortical synaptic terminations (Nahmani and Erisir, 2005) (Figure 1B).

Sixty-four-electrode eCoG recordings of dCx responses to flashed stimuli in awake animals showed that the visually responsive zone in dCx matches that revealed by WGA-HRP tracing experiments (Figure S1). Visually evoked local field potential (LFP) activity extended over several square millimeters in the rostral half of the cortex. eCoG traces revealed dominant spectral power in the beta range (15–35 Hz; Figure 1D), plotted as iso-amplitude contours in Figure 1E. The extent of the visually activated zone did not depend on the spectral band selected to analyze the data.

We used this knowledge to target our depth recordings in anesthetized turtles to area D2 (as confirmed post hoc from VGluT2 stainings). Current-source density profiles measured across the depth of dCx in anesthetized animals revealed an early (<100 ms) superficial current sink (Figure 1C, middle) whose

depth profile matched the zone of LGN afferent projections (Figure 1C, left).

Oscillatory Dynamics and Population Phase-Locking in Response to Visual Inputs

The macroscopic (LFP or eCoG) responses of turtle visual cortex to visual stimuli typically contained an early, stimulus-locked broadband component and a superimposed and sustained oscillatory component. We observed these oscillations for a variety of stimuli both in anesthetized animals (Figure 1F) and in awake animals (Figures 1D and 1E). Consistent with earlier reports (Prechtl et al., 1997; Rutishauser et al., 2013; Senseman and Robbins, 1999), the power increase in the stimulus-evoked oscillations was strongest in the beta range (15–35 Hz). We observed a peak oscillatory power between 15 and 25 Hz (anesthetized, mean = 19 Hz, range = 15–25 Hz, $n = 5$ animals; awake, mean = 23 Hz, range = 22–25 Hz, $n = 4$ animals).

To examine the potential significance of the macroscopic oscillations in determining the timing of neuronal responses, we recorded cortical LFPs together with the responses of individual neurons to visual stimuli (sparse and dense noise; STAR Methods) using linear silicon arrays inserted across the entire cortical depth in anesthetized animals (Figures 1F–1H). On average, beta LFP oscillations (triggered on the oscillation trough recorded from a superficial channel) showed almost no gradient of phase across depth, but a rapid phase reversal superficially, at a level corresponding approximately to the transition between layers 1a (containing LGN axon terminals) and 1b (Figure 1G).

Beta oscillations measured in the LFP reflected the firing statistics of the neuronal population in dCx (Figure 1H). The correlation between spike times and LFP was quantified by computing the peri-oscillation-triggered histogram (POTH; STAR Methods). In total, 65% of the recorded neurons (479 out of 741) showed a significant modulation of their firing rate across a beta oscillation cycle (Rayleigh test, $p < 0.01$). For some neurons, this oscillatory activity was clearly reflected in their spike autocorrelogram (Figure S2). These neurons preferred to fire in the descending phase of the beta oscillation cycle (Figure 1H, middle), indicative of synchronous excitation. Note that ~30% of these neurons exhibited less than 20% firing rate modulation during an oscillation cycle (Figure 1H, right).

(C) Comparison of the dCx layered structure and a typical CSD profile. Left: cross-section of dCx as in (A), revealing the different layers. Scale bar, 100 μ m. Middle: depth profile of CSD in one anesthetized animal, scaled as in left panel. Blue, sink; red, source. Right: averaged stimulus-triggered LFPs, recorded with 32-channel linear probe.

(D) Top: single-trial dCx activity (unfiltered, black; band-pass [15–35 Hz], blue) evoked by a static stimulus (2 s natural image; onset indicated by the arrow), recorded in awake turtle with an eCoG array using the channel with the largest oscillations in the beta range (indicated by an asterisk in E, top).

(E) Iso-amplitude contours of oscillatory power (15–35 Hz band) recorded with eCoG grid in response to natural scenes (top), and location of eCoG responses across dCx (bottom). dCx, dorsal cortex; ICx, lateral cortex; OB, olfactory bulb; rf, rhinal fissure; T, tectum; th, thalamus. Scale bar, 1 mm. See also Figure S1.

(F) Top: single-trial spiking responses of sorted units (SU) together with simultaneously recorded LFP (unfiltered, black; band-pass [15–35 Hz], blue) evoked by a 1 s static stimulus (sparse noise, onset indicated by the arrow). Bottom: average time-frequency plot of LFP power recorded from a superficial channel around current sink peak, in response to a 1 s-long flashed stimulus (sparse noise, gray line). Oscillatory power is normalized to the spontaneous activity recorded before stimulus onset.

(G) Average depth profile of beta LFP oscillations (15–35 Hz) measured along a 32-channel linear array, by triggering on the trough of the oscillation of the superficial channel corresponding to the current sink peak (same channel as in F).

(H) Left: example of peri-oscillation-triggered histogram (POTH, black) normalized to mean firing rate of that neuron (spike rate modulation). Blue: POT LFP of the channel used to measure spike times (from trough). Middle: distribution of preferred firing phase across neurons that showed significant POTH modulation. Right: distribution of the maximum spike rate modulation (spike rate normalized to mean firing rate, i.e., maximum of the POTH in left panel) for neurons that showed significant POTH modulation (Rayleigh test, $p < 0.01$). See also Figure S2.

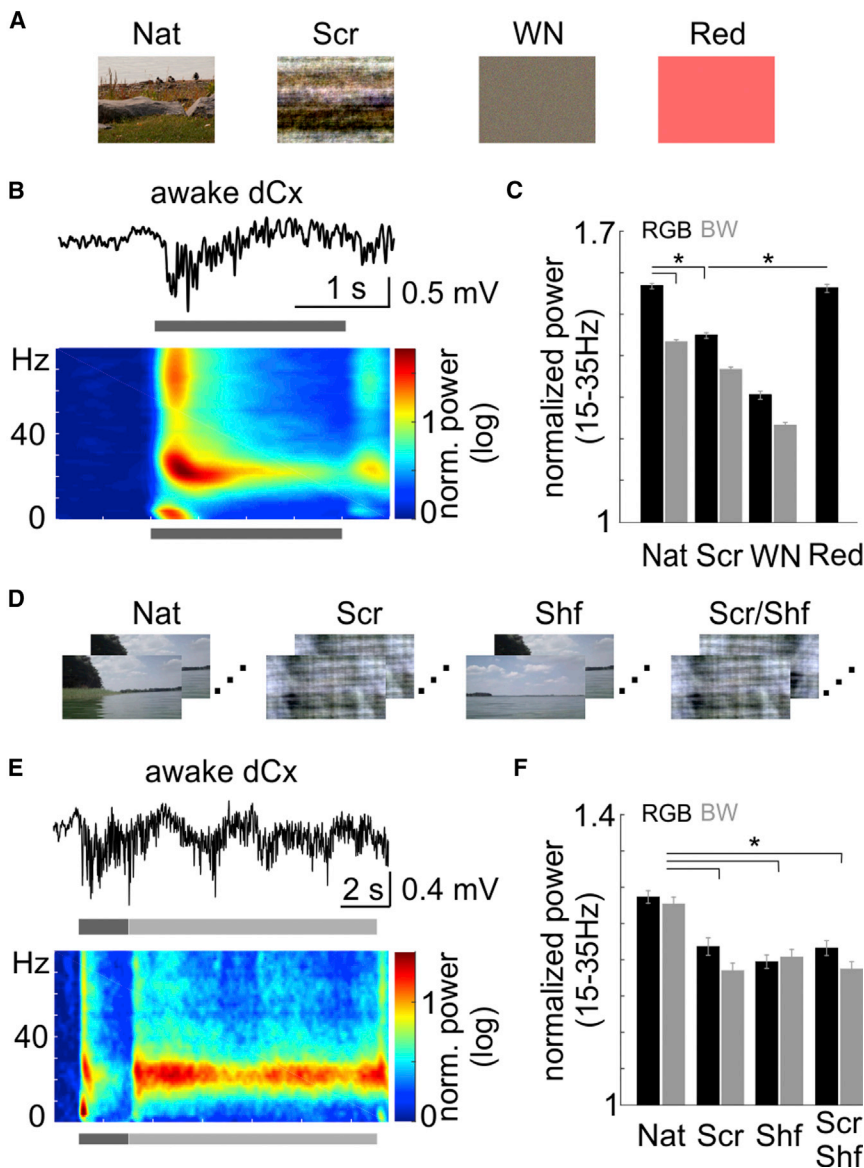


Figure 2. dCx Response to Natural Images and Movies in Awake Animals

(A) Examples of static stimuli used to probe visual responses in dCx of awake turtle. Static stimuli were taken from a total of 320 different images (each in RGB or grayscale [BW]; natural, Nat; natural + phase-scrambled, Scr; noise, WN; uniform, red; STAR Methods). Images were each presented for 2 s in pseudorandom order, with ~10 s interval (uniform gray background) between stimuli.

(B) Top: single-trial eCoG response to a natural image recorded from one site. Bottom: corresponding average time-frequency spectrogram normalized to spontaneous-activity power.

(C) Comparison of oscillatory response intensity (in 15–35 Hz band) across static stimulus classes. Oscillatory power was normalized to spontaneous activity for each animal. Error bars are \pm SEM. Responses for different stimulus classes were significantly different (ANOVA, $p < 0.01$), except between RGB natural image and uniform (red) flashes and grayscale natural images (BW Nat) and scrambled RGB images (RGB Scr).

(D) Natural movie stimuli consisted of 10 s-long video clips; frame 1 was shown for 2 s before transitioning to following ones (20 fps [frames per second] thereafter). In manipulated movies, the spatial structure and/or the temporal sequence of the movie frames was modified (Scr, Shf, and Scr/Shf; STAR Methods).

(E) Same as in (B), for RGB natural movies. Note sustained oscillatory power in the beta range throughout movie.

(F) Comparison of oscillatory responses (15–35 Hz) across movie stimuli. Response amplitude was measured as oscillatory power evoked after movie onset, averaged across entire clip duration. Oscillatory power was normalized to spontaneous-activity power spectrum for each animal. Error bars are \pm SEM. Responses were significantly higher for the natural movie (RGB or grayscale) compared to when the movie frames were scrambled and/or shuffled (ANOVA, $p < 0.01$). See also Figure S3.

Sensitivity to Spatial Features in dCx of Awake Turtles

To examine whether dCx is sensitive to the spatial structure of visual stimuli, we examined the effectiveness of various stimulus categories in driving beta activity in awake animals ($n = 4$). Using a large set of luminance-adjusted static images (Figure 2A; STAR Methods), we measured power in the beta range (15–35 Hz; Figures 2B and S3) for each stimulus and category. The most efficient stimulus categories were RGB natural scenes and uniform red flashes (Figure 2C). Least effective were phase-scrambled BW scenes and white-noise stimuli. The high effectiveness of red stimuli is likely explained by the known bias of the turtle retinal spectral sensitivity (Graf, 1967), but the ranking across the remaining stimuli suggests a sensitivity of turtle cortex activity to the spatial structure of the image. In particular, the significant preference for natural images (Nat) compared to their phase-scrambled counterparts (Scr) (ANOVA, $p < 0.01$) indi-

cates that dCx may be selective to the presence of salient contours.

Using movies of natural images, we also found that dCx is sensitive to the spatiotemporal statistics of the visual scene. eCoG responses evoked by 10 s-long natural movie clips (Figure 2D) showed increased power in the beta range upon static presentation of the first frame (Figure 2E, dark gray) and at the movie onset (2 s later), but also sustained beta oscillations throughout the entire movie (Figures 2E and S3). Sustained beta oscillations measured after movie onset were significantly smaller when the frames of the movie were phase-scrambled (Scr) and/or shuffled in time (Shf) (ANOVA, $p < 0.01$; Figure 2F; $n = 2$ animals; STAR Methods).

Absence of Fine Retinotopy in dCx

To test whether RFs are organized retinotopically across dCx, we recorded the activity of dCx neurons extracellularly in

anesthetized and paralyzed turtles and measured their spatial selectivity with “sparse-noise” stimuli consisting of bright (ON) or dark (OFF) squares flashed on an intermediate intensity background (3 × 5 positions covering 90° × 120° of visual angle; STAR Methods; Figure 3A). Consistent with earlier reports (Gusel'nikov et al., 1972; Mazurskaya, 1973), we found that the population response (MUA) recorded in any of the dCx locations we sampled covered the entire stimulated area. Responses to sparse noise recorded simultaneously in two different sites, spaced by >1 mm along the rostro-caudal axis of dCx (n = 3 out of 5 animals), were highly similar, with no obvious spatial anisotropy in RF location across the dCx surface (Figures 3A and S4A). Nevertheless, we measured a temporal delay across dCx recording sites: caudal dCx average responses were delayed by ~30 ms compared to rostral dCx (Figure 3B, bottom; mean = 32.2 ms; paired t test, $p < 0.01$), consistent with earlier reports on propagation of activity across dCx (Senseman, 1999). Moreover, we found a significant correlation between the latency of dCx responses and the azimuthal position of the stimulus for individual recording locations: on average, responses to single flashes in the periphery of the visual field were delayed by ~70 ms compared to the center (Figure 3B, top; $r = -0.78$, $p < 0.01$). This result suggests the possibility that azimuth of the visual field may be encoded in the timing of dCx responses.

Retrograde tracing from dCx recording sites revealed a retinotopic organization of thalamocortical projections that was very coarse at best. We routinely coated our recording electrodes with lipophilic dyes (Figure 3C; STAR Methods). These dyes underwent retrograde axonal transport and, thus, identified thalamic afferents. After 1–4 weeks, LGN neurons labeled retrogradely from the dCx recording site (STAR Methods) were detected over most of the rostro-caudal axis of LGN (Figures 3D–3F). Quantitative analyses reveal that rostral dCx (Figure 3E, light brown) receives inputs from cells distributed throughout the whole rostro-caudal extent of the LGN, while more caudal portions of dCx (Figure 3E, dark brown) gradually lack input from caudal LGN. Applying two different tracers along the rostro-caudal axis of dCx (DiI and DiD) revealed large spatial overlap in LGN, but only very few (<2%) double-labeled cells (Figure 3E, inset). These results indicate coarse differences between (rostral to caudal) LGN projections along the rostro-caudal axis of dCx. Yet the widespread divergence of LGN output to any part of dCx is consistent with the absence of a fine-grain retinotopic organization of dCx, as indicated by our electrophysiological recordings.

Receptive Fields and Encoding of Position and Contrast in dCx

To assess the diversity of spatial selectivity across the dCx neuronal population, we quantified the RF properties of individual dCx neurons from responses to sparse noise in anesthetized turtles. Most recorded neurons responded over large parts—often all—of the stimulated area. Significant responses were observed in ~75% of the recorded neurons over more than 90% of the explored visual area (i.e., more than 100° of visual angle) (Figures 4A and 4B; n = 128 neurons and 5 animals). Moreover, ON and OFF subfields usually overlapped in a given neuron, as shown by the correlation coefficient measured be-

tween ON and OFF responses (Figure 4C, middle). No systematic bias was found between ON and OFF responses (paired t test, $p = 0.75$; Figure S4B).

Despite their large size, dCx RFs are not entirely uniform across space. The spatial modulation index showed that 50% of neurons (70/128) had more than 20% modulation of their response amplitude across space (Figure 4C, left; median = 0.21). Cells with RF size <100° of visual angle showed larger spatial modulation (Figure S4C; median = 0.28; n = 34 neurons) than cells with large RFs (>100° of visual angle, n = 94; median = 0.18). Moreover, ON and OFF responses were not perfectly balanced across the visual field for most neurons: the correlation between ON and OFF responses was <0.6 for ~50% of dCx neurons (median = 0.62) (Figure 4C, middle); i.e., half of dCx neurons show more than ~40% modulation of their response to contrast of opposite signs.

Additionally, RFs were not uniform within local populations of dCx neurons. We measured the Pearson's correlation between every neuron's RF and the mean RF averaged across all other neurons recorded simultaneously on the same electrode (Figure 4C, right; population correlation). For half of dCx neurons, this correlation was <0.4 (median = 0.40); i.e., more than ~60% of the variance of their RFs could not be explained by the average response from the rest of the population. We also compared the uniformity of RFs across recording sites separated along the rostro-caudal dimension by measuring the Pearson's correlation between RFs recorded in rostral (or caudal) dCx and the mean RF averaged across neurons recorded in caudal (or rostral) dCx (n = 3 animals). Comparison of population correlation values within and across recording sites showed that dCx RFs tended to be more uniform within the local population (Figure S4D; paired t test, $p < 0.01$).

To assess whether the diversity of RFs across the dCx population was sufficient to decode the position and polarity of the stimulus, we used a Bayesian decoding approach and measured the average posterior probability from the recorded spike trains for each stimulus position and contrast (STAR Methods). Both the location and the ON or OFF polarity of the stimulus could be decoded from dCx neuron responses (Figures 4D and S4E). Thus, despite their poor spatial selectivity, dCx neurons exhibit some anisotropy in their spatiotemporal response profiles, which can be used to decode the location and contrast polarity of a stimulus.

Encoding of Stimulus Position during Prolonged Stimulation

Responses in dCx are usually much reduced during prolonged stimulation (Clawson et al., 2017). To test if positions in the visual field are also encoded in dCx responses during ongoing stimulation, we recorded the activity of dCx neurons in anesthetized turtles during the presentation of an ~30 s-long movie clip, displayed in different positions on the screen (Figure 5). Unlike sparse noise stimuli, the luminance of each movie frame was adjusted to the background luminance and all movie frames were equalized in overall contrast.

Across all experiments (n = 123 neurons and 4 animals), most neurons responded reliably to the appearance of the first frame and to the onset of the movie in all stimulated positions

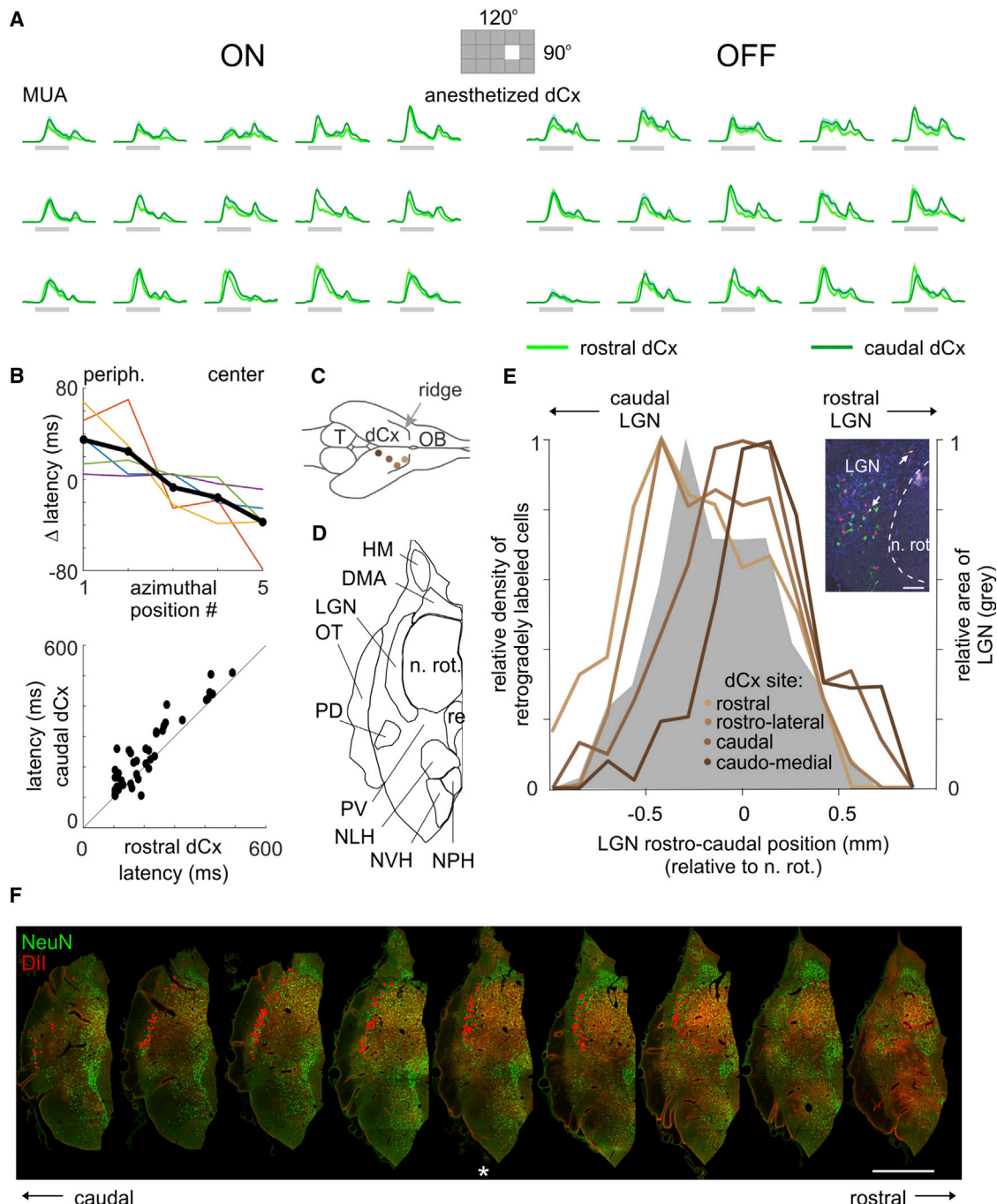


Figure 3. Absence of Fine Retinotopic Mapping in dCx

(A) ON (left) and OFF (right) RFs (\pm SEM) estimated with sparse noise from population responses (MUA) recorded simultaneously in one anesthetized animal from two distant rostrocaudal dCx sites (rostral, light green; caudal, dark green). ON and OFF response profiles were normalized to their maximum firing rate across all positions. Stimulus duration (1 s) is indicated by the gray line.

(B) Top: latency of rostral dCx responses to sparse noise flashes as a function of the azimuthal position of the stimulus, expressed relative to the mean latency. Latency was measured at the first crossing of 50% of the maximum firing rate, after averaging ON and OFF responses across vertical positions. Colored lines correspond to single recordings ($n = 5$ animals). Bottom: comparison of response latencies between rostral and caudal dCx recording sites ($n = 3$ animals; 3×5 positions per animal).

(C) Position of the Dil- or DiD-coated electrodes, used for analysis in (E). Each color corresponds to a different experiment. dCx, dorsal cortex; OB, olfactory bulb; T, tectum.

(legend continued on next page)

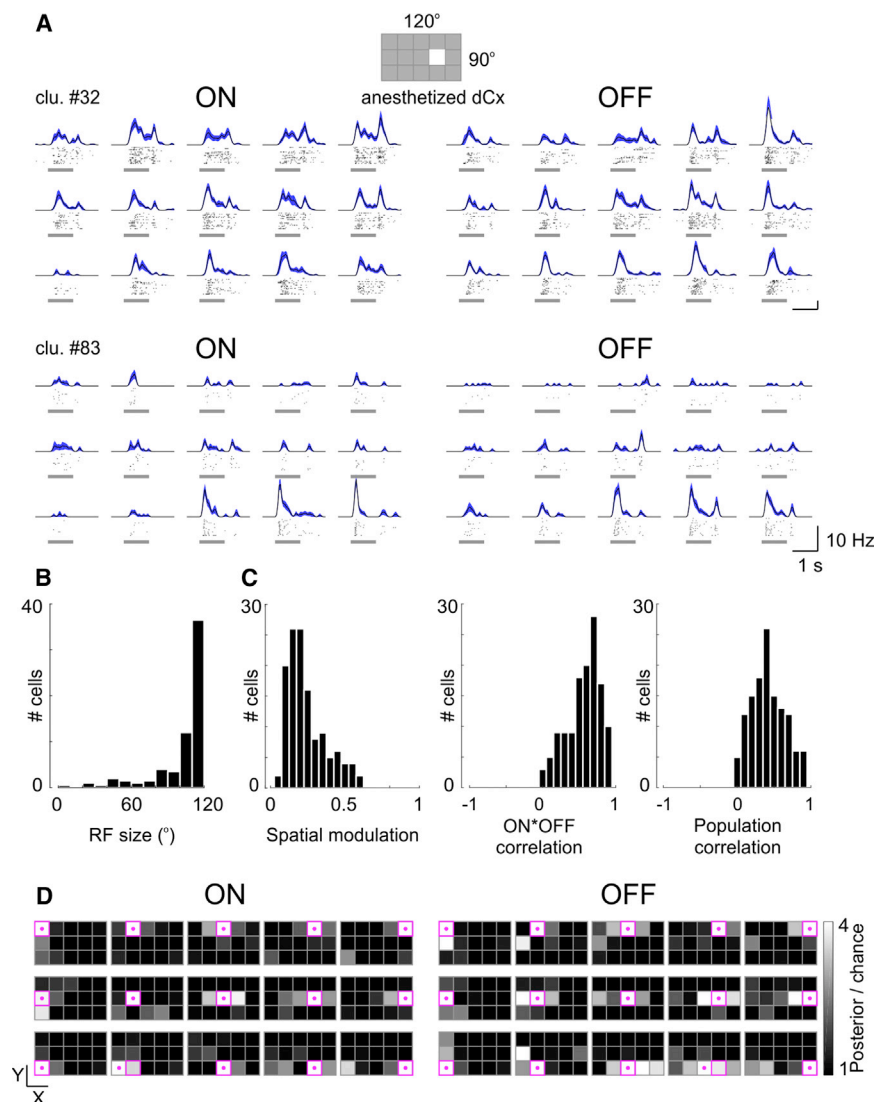


Figure 4. Encoding of Stimulus Positions in dCx Responses to Sparse Noise

(A) ON (left) and OFF (right) RFs (\pm SEM, blue) mapped with sparse noise for two spike-sorted neurons (clu.) recorded simultaneously in an anesthetized turtle. These two neurons illustrate the range of RF sizes observed across the population. Stimulus duration (1 s) is indicated by a gray line under each raster. The position of each raster in each 3×5 matrix indicates that of the corresponding stimulus on the screen (see inset).

(B) Distribution of spatial extent of dCx RFs, measured as the average of ON and OFF subfields ($n = 128$ cells, 5 animals).

(C) Left: distribution of the spatial modulation index (STAR Methods). Middle: distribution of the correlation coefficient between ON and OFF responses. Right: distribution of the population correlation, measured as the Pearson's correlation between a neuron RF and the mean RF averaged across all other neurons recorded simultaneously (STAR Methods).

(D) Sparse noise stimuli were decoded from dCx neuron responses using a Bayesian approach (STAR Methods). The posterior probability was averaged across trials for each position (indicated by the magenta square in each matrix) and contrast polarity (left, ON; right, OFF). The amplitude of the posterior is expressed relative to chance level (i.e., chance = $1/(\#X_{pos} \times \#Y_{pos} \times \#contrast) = 1/30$). The position of the maximum of the posterior is indicated by a magenta dot. The 3×5 grid of the sparse noise is indicated by the thin gray lines. The presented maps correspond to averages across all experiments ($n = 5$ animals). See also Figure S4.

(Figures 5A and S5). Similar to sparse noise, responses to the onset of the movie were not entirely uniform across space or across the dCx population: 50% of dCx neurons modulated their responses across space by more than $\sim 20\%$ (Figure 5B, left; median = 0.18) and more than 60% of their RF variance could not be explained by the average response of all other cells (Figure 5B, right; population correlation; median = 0.38). To test if the

location of the movie could be decoded from the response of dCx neurons at the movie onset, we applied the same Bayesian approach as above. Similar to results with sparse noise, we found that the position of the movie could be accurately decoded from the activity recorded in dCx for the first 4 s following stimulus onset (Figures 5C and S6A), although most neurons exhibited significant responses to all stimulated positions (Figures S5A and S5B).

After movie onset, the firing rate of most dCx neurons decreased drastically (Figures 5A, S4A, and S4B). Nevertheless,

(D) Thalamic nuclei are delineated on one section example (referring to section marked with an asterisk in F). HM, n. habenularis medialis; DMA, n. dorsomedialis anterior; LGN, lateral geniculate nucleus; n.rot., nucleus rotundus; OT, optic tract; PD, n. pedunculus dorsalis; PV, n. pedunculus ventralis; re, n. reuniens; NLH, n. lateralis hypothalami; NVH, n. ventralis hypothalami; NPH, n. periventricularis hypothalami (Powers and Reiner, 1980).

(E) Rostro-caudal distribution of LGN neurons retrogradely labeled from the dCx cortical sites indicated in (C). Analysis was restricted to dye deposits revealing >500 retrogradely labeled cells. Rostral positions in dCx result in labeling along the entire extent of LGN, with the local number of retrogradely labeled cells varying with LGN area (compare to gray shaded area, representing the area of LGN measured in one animal example). More caudal dye deposition reveals a successive lack of labeled cells in caudal LGN. Distributions were aligned to the maximum area of nucleus rotundus (n. rot.), the most reliable landmark in thalamus. Inset: simultaneous retrograde tracing from two sites in dCx, separated by >1 mm in the rostro-caudal dimension, reveals overlapping regions of labeling. However, only a small fraction of cells ($<2\%$) are double labeled (arrows).

(F) Dil retrograde labeling of thalamic neurons from one cortical recording site in dCx (corresponding to the second most rostral position in C). Presented sections span the entire extent of LGN from caudal (leftmost) to rostral (rightmost) every $140 \mu\text{m}$. Retrogradely labeled neurons, identified in confocal image stacks, are indicated with a red dot. Scale bar, 1 mm.

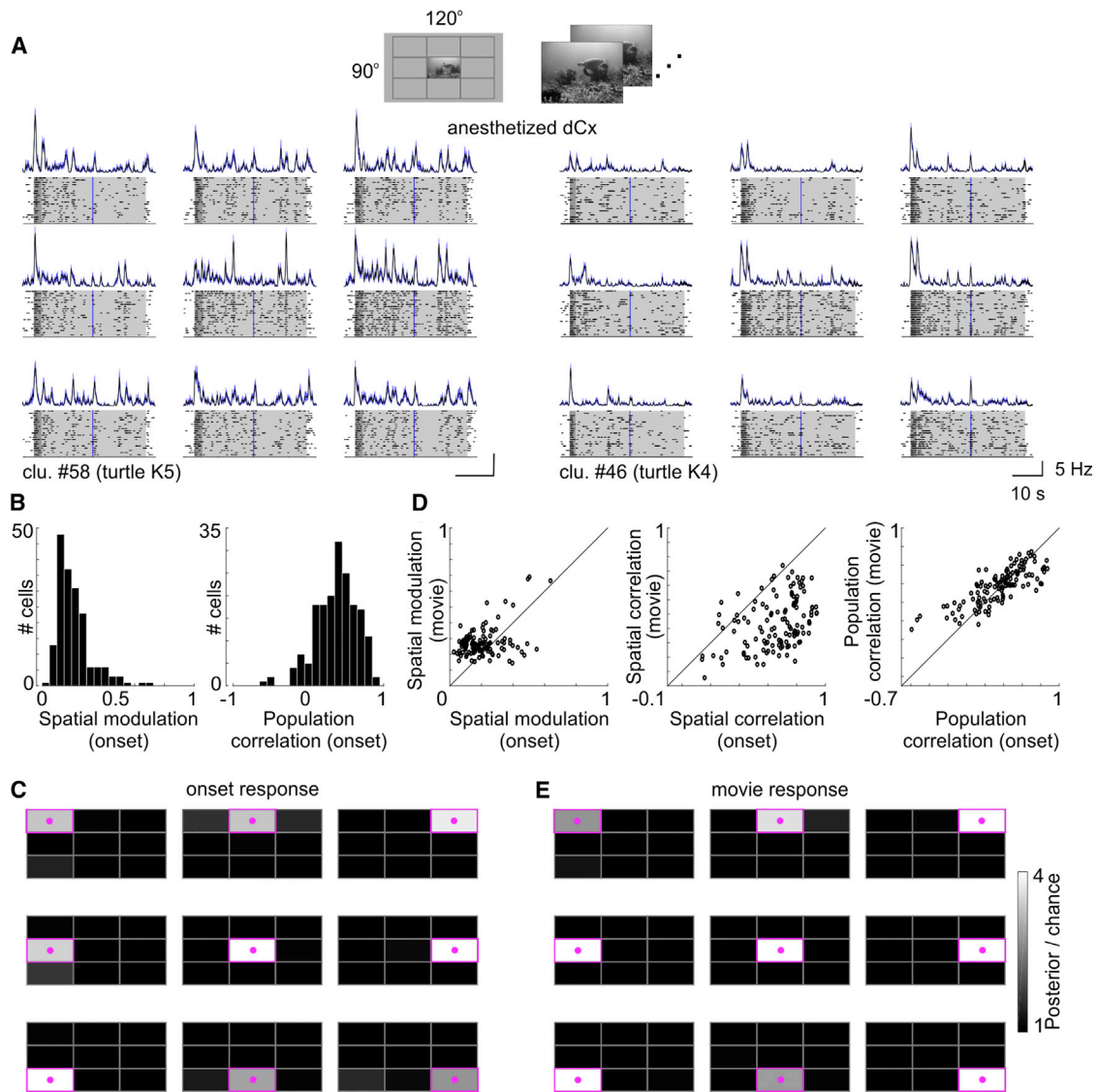


Figure 5. Encoding of Stimulus Position in dCx Neural Responses to Natural Movies

(A) Responses to natural movie stimuli. Movie stimuli used in the anesthetized animal consisted of a 2 s-long presentation of the first movie frame, followed by two successive presentations of the full movie at 20 fps (~36 s in total). The movie was presented in one of nine locations of the screen in a pseudorandom sequence. The relative position of each block of trials corresponds to the position of the stimulus on the screen. Top traces are PSTHs (mean in black; SEM in blue).

(B) Left: distribution of the spatial modulation index of dCx RFs, measured from the responses to the movie onset (i.e., using the first 4 s following stimulus onset) ($n = 123$ cells, 4 animals). Right: distribution of the population correlation from onset responses, measured as the Pearson's correlation between a cell response and the mean response averaged across all other cells recorded simultaneously (STAR Methods).

(C) The position of the movie was decoded using a Bayesian approach (STAR Methods) from dCx neuron responses to the first 4 s following stimulus onset ("onset response"). The posterior probability was averaged for each position (indicated by the magenta rectangle in each matrix). The amplitude of the posterior is expressed relative to chance level. The maximum of the posterior is indicated by a magenta dot for each stimulus position. The shown posterior probability corresponds to average across all experiments ($n = 4$ animals).

(D) Left: comparison of the spatial modulation index measured from responses to movie onset (same as in B) and to movie presentation (from 4 s post-onset until the end). Middle: comparison of the coefficient of spatial correlation of the RF measured from responses to movie onset and to movie presentation. The coefficient of spatial correlation was measured as the average coefficient of correlation between the response of a neuron in a given position and the mean response of the same neuron averaged across all other positions. Right: comparison of the population correlation computed from responses to movie onset and to movie presentation.

(E) Decoding of the position of the movie from dCx neuron responses to the movie presentation ("movie response"). Same method as in (C). The amplitude of the posterior is expressed relative to chance level. The maximum of the posterior is indicated by a magenta dot for each stimulus position. The shown posterior probability corresponds to average across all experiments ($n = 4$ animals). See also Figures S5 and S6.

responses, if present during the movie, were clearly structured (Figures 5A and S5). Some response peaks were correlated with the transition between the last frame of run 1 of the movie and the first frame of run 2 (blue line), while some others were locked to specific features of the movie, possibly related to increased visual flow (Figures S5A and S5B). Responses during the movie presentation (from 4 s post-onset till the end of the movie) were more spatially selective than at the onset of the stimulus as shown by the higher spatial modulation index (Figure 5D, left; paired t test, $p < 0.01$). The coefficient of spatial correlation of the RF was also significantly lower during the movie presentation (median = 0.31) than at the stimulus onset (median = 0.70) (Figure 5D, middle; spatial correlation, paired t test, $p < 0.01$; STAR Methods), indicating that dCx neurons exhibited more position-specific responses during the movie presentation. The correlation between responses recorded from different neurons (population correlation) was unchanged compared to the correlation between responses recorded at the onset of the stimulus (Figure 5D, right; paired t test, $p = 0.19$). Thus, while the firing rate of dCx neurons decreases during stimulation, their spatial selectivity increases. This result is consistent with recent findings suggesting a trade-off in dCx between detection and discrimination as the response develops following stimulus onset (Clawson et al., 2017). Bayesian decoding of the stimulus position from responses recorded during the movie showed that the position of the stimulus can also be decoded during prolonged stimulation, despite the strong adaptation of dCx firing rates (Figures 5E and S6A).

In one experiment (turtle K5), we presented three different movies during the same recording session (Figures S5B and S5D). Bayesian decoding of the stimulus from responses recorded either at the onset or during the movie presentation showed that both the position and the identity of the movie could be decoded from dCx activity (Figure S6B), suggesting that visual features other than position and contrast polarity are likely encoded across the dCx population.

Linear and Nonlinear Components of dCx Receptive Fields

The large overlap measured between ON and OFF subfields with sparse noise suggested that the nonlinear RF component often dominated the evoked response (Figure 4C, middle). Sparse stimuli did not seem appropriate to extract reliable linear components: the estimated ON-OFF linear RFs were often noisy and barely statistically significant (Figure S7).

Inspired by the finding that dense stimulation is more effective in cat V1 to estimate linear RFs (Fournier et al., 2011), we recorded responses to dense-noise checkerboard stimuli in anesthetized turtle dCx ($n = 561$ neurons, 20 recording sessions in 5 animals) and dissected out RFs into linear and nonlinear components to assess their respective spatial selectivity. RFs were computed using the stimulus-contrast derivative (Figure 6A). Linear and nonlinear components of dCx RFs were estimated using a least-squares method (STAR Methods). In this framework, the linear RF of a neuron corresponds to the component that contributes linearly to that neuron's response; the nonlinear RF describes the component of the response that does not depend on the sign of the contrast derivative. Across

our cell population, this RF model could explain $\sim 35\%$ of the variance of the responses (mean = $37\% \pm 9\%$ SD, $n = 561$). Figure 6B illustrates the linear and nonlinear RF components of two representative neurons recorded simultaneously. While their nonlinear RFs contained little spatial structure, their linear RFs revealed an interesting spatial anisotropy (Figure 6C). In neuron #6, the linear RF showed ON and OFF subfields arranged side by side, reminiscent (in structure, but not in size) of oriented RFs of simple cells in mammalian V1 (Hubel and Wiesel, 1962). By contrast, the linear RF of neuron #14 revealed a dominant OFF response decaying from center to periphery. Over the population, the nonlinear RFs almost always extended over the entire stimulated area, with little spatial modulation; the linear components were usually more restricted and spatially modulated (Figures 6D and 6E). The linear RFs generally represented a small fraction of the total RF energy (Figure 6F, linear RF index; median = 0.06). By analogy with neurons in mammalian V1, one might therefore consider that all dCx neurons are complex-like neurons.

While a majority of dCx RFs had no selective component in the orientation domain (as defined by a maximal power for null spatial frequencies in their 2D power spectrum; Figure 6C), 37% of dCx RFs (206 out of 561) had a linear component that was spatially oriented. For these cells, we measured the orientation of the linear RF at the time of maximal response by convolution with gratings of different orientations at best spatial frequency (as measured from the 2D power spectrum). The orientation selectivity index (OSI) measured from the estimated tuning curves revealed a wide range of orientation selectivity in dCx and most linear RFs had an OSI < 0.5 ($\sim 70\%$, 146/206; Figure 7A), i.e., less than 50% modulation of their response to orthogonal gratings. But some neurons (with OSI > 0.3 , $\sim 60\%$, 126/206) had a clearly spatially oriented organization of their linear RFs (Figures 7C–7E). The linear RFs of these cells were more often oriented along the horizontal axis of the visual field across our cell population (Figure 7B). This bias could be related to the presence of an elongated area centralis (“visual streak”) in the retina, which contains the highest density of ganglion cells, and which turtles actively maintain facing horizontally (Brown, 1969).

Spatially Selective Adaptation

One characteristic feature of visually evoked responses of dCx neurons is a prominent adaptation to repetitive stimulation, resulting in a complete extinction of the evoked responses after a few stimuli at interstimulus intervals (ISIs) shorter than several seconds (typically < 5 s; Gusev'nikov and Pivovarov, 1978; Gusev'nikov et al., 1972; Hayes et al., 1968; Luo et al., 2010). To assess the spatial selectivity of this adaptation, we recorded, in anesthetized turtles, responses of dCx neurons to sparse noise stimuli in which one of the positions (adapting position) was more frequently stimulated than the others (test positions; $P(\text{adapting}) = 0.9$; Figure 8A). Responses measured in this condition were compared to control responses measured with long ISI (> 10 s). Although evoked responses to the most frequently stimulated position completely disappeared within a few presentations, dCx neurons still responded to the other spatial positions, which were less frequently

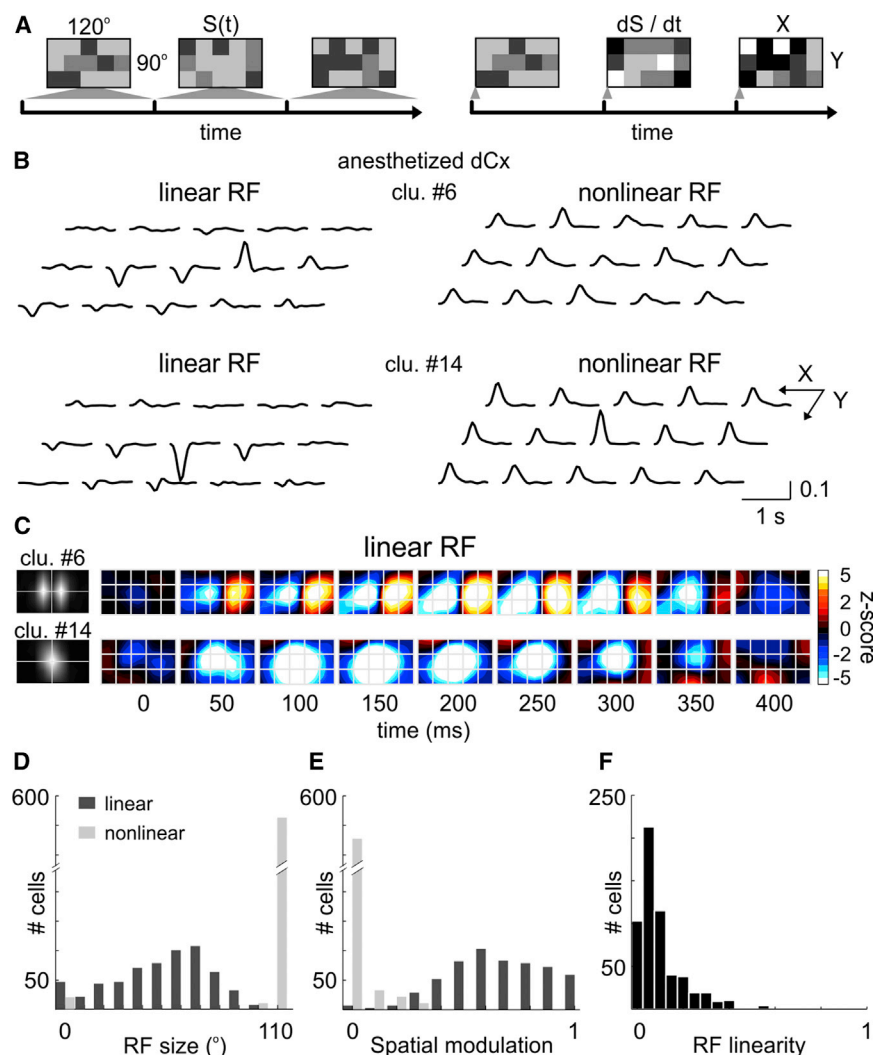


Figure 6. Linear and Nonlinear Receptive Field Components in dCx

(A) Left: dense noise stimulus (luminance $S(t)$). Right: derivative of the stimulus contrast used to estimate RFs.

(B) Linear (left) and nonlinear (right) RF components for two cell examples recorded simultaneously in an anesthetized animal.

(C) Z scored spatial profile of the linear RF component at different times following stimulus onset (same neurons as in B). The leftmost plots show the spatial power spectrum at time of maximal response.

(D) Distribution of RF size across the sampled neuron population for the linear (dark gray) and nonlinear (light gray) components.

(E) Distribution of the spatial modulation index measured from linear (dark gray) or nonlinear (light gray) RF components (computed as 1 minus the proportion of variance explained by the spatial average of the RF; STAR Methods).

(F) Distribution of the RF linearity index across our cell population (proportion of RF energy contained in the linear component; STAR Methods). See also Figure S7.

stimulated (Figures 8B, 8C, and S8A–S8E). This adaptation was reversible and could be elicited at all tested locations (Figures S8C–S8E). Thus, adaptation to repeated stimulation in dCx is spatially specific.

We investigated how this adaptation depended on spatial distance by presenting vertical bars (20° width each) that overlapped with the adapting central bar by 75% to 0% (25% decrements, i.e., 5° displacements in both directions). Comparison of RFs measured in the adapting and control conditions showed that adaptation was almost linearly related to the spatial overlap of test stimuli with the adapting stimulus (Figures 8D and 8E).

Analysis of current source density (CSD) profiles from depth recordings in anesthetized turtles during adapting and control conditions showed that the superficial current sink completely disappeared in response to the adapting stimulus (Figure 8F). If one assumes that this sink of current reflects, at least in part, the depolarization caused by thalamic afferents, this result suggests that adaptation to repeated stimulation is associated with a decrease of the thalamic drive to dCx. This could be

due either to adaptation of LGN neurons or to synaptic depression at thalamocortical synapses. To test for the former hypothesis, we measured responses of LGN neurons to adapting stimulation sequences in an *ex vivo* eye-brain preparation (STAR Methods). Although single units in LGN showed a moderate decrease in their evoked response between control and adapting conditions, we found no evidence for a spatially selective component of this adaptation over the LGN neuronal population

(Figures 8G and S8F–S8H). Therefore, we conclude that spatially selective adaptation in dCx most probably results from depression of sensory afferent synapses. Finally, we measured surface eCoG responses to adapting stimulation in awake turtles ($n = 2$ animals). We found that adaptation to repeated stimulation in the same location with an ISI of 2 s also resulted in a spatially restricted decrease of dCx responses, demonstrating the relevance of this feature of dCx visual processing in the awake animal (Figure 8H).

DISCUSSION

As in mammalian V1, visual afferents to turtle dCx reflect a disynaptic pathway from the retina, relayed in the LGN; however, thalamocortical projections are not clearly organized retinotopically (with the exception of a slight rostro-caudal projection gradient) and visual responses from neurons anywhere in dCx can be elicited from the entire visual field. In this context, our finding that spatial features of a visual scene can be extracted from population and single-neuron activity comes as a surprise.

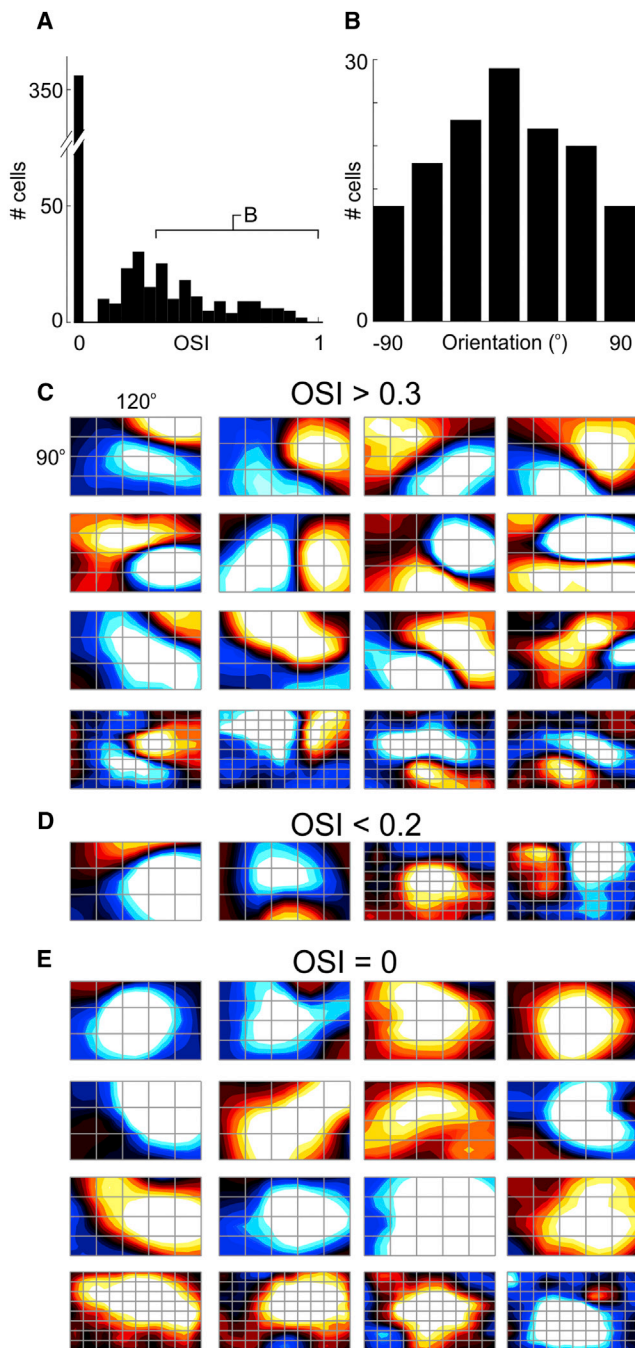


Figure 7. Orientation of dCx Linear Receptive Fields

(A) Distribution of the orientation selectivity index (OSI) measured from dCx linear RF components. Neurons with OSI = 0 had power spectrum maximum at $(fx, fy) = (0, 0)$.

(B) Distribution of the orientation of dCx linear RF components for neurons with OSI > 0.3 (see in A). Zero-degree orientation corresponds to horizontal.

(C) Spatial profile of the linear RF component at time of maximal response for 16 neurons with OSI > 0.3 (same color scale as in Figure 6C).

(D) Same as in (C) for four cells with $0 < \text{OSI} < 0.2$.

(E) Example of linear RF components classified as non-oriented (OSI = 0). The grid of the dense noise is indicated by the thin lines.

Spatial Information Encoded in Turtle Cortical Population Activity

Visual responses to diffuse or localized flashes of light were reported in dCx over 40 years ago (Gusel'nikov et al., 1972; Mazurskaya, 1973; Mazurskaya et al., 1967). Examining eCoG responses to different stimulus classes in awake animals, we found that dCx is sensitive to the spatial and temporal structure of natural images and movies, suggesting that dCx neurons encode spatial and temporal information about the visual scene.

Using RF mapping, we showed that the vast majority of RFs in turtle dCx cover a large fraction, if not all, of the contralateral visual field. The large size of dCx RFs is not the result of a poor visual acuity: previous recordings from the optic tectum showed that the visual acuity of freshwater turtles ranges from 4 to 10 cyc.deg⁻¹ (Northmore and Granda, 1991), consistent with the spacing of retinal ganglion cells measured in the area centralis ("visual streak") (Peterson and Ulinski, 1979).

However, not all RFs cover the entire hemifield uniformly and the latency of dCx responses increases from nasal to temporal visual field. Bayesian decoding of responses to sparse noise and natural movies showed that dCx neuron activity can be used to decode both position and contrast polarity of a stimulus. Therefore, despite the low spatial selectivity of their RFs, dCx neurons may, as a population, still encode spatial position with some accuracy, suggesting a representation of visual space distributed across the entire visual cortex. Because of the large size of our test stimuli (imposed by methodological constraints; STAR Methods), we cannot yet determine the true accuracy of spatial processing in dCx at a resolution lower than ~30° of visual angle.

Sensory representation in dCx appears to differ fundamentally from those in the amniote optic tectum and mammalian V1. Unlike what has been extensively described in mammalian V1, visual processing in turtle dCx does not seem to rely on a clear parametric analysis of visual features but rather takes the form of a distributed encoding of the visual scene across the entire network. Coding in dCx thus appears more similar to that in other cortical areas, such as olfactory (Bolding and Franks, 2017; Miura et al., 2012; Roland et al., 2017) or inferotemporal cortices (Desimone et al., 1984; DiCarlo et al., 2012; Hung et al., 2005; Kiani et al., 2007), where stimuli can also be decoded from populations of broadly tuned neurons (for review, see Quiñero and Panzeri, 2009). It suggests that processing of spatial information in dCx might be used for high-order analyses of visual scenes (e.g., to represent relative locations of features within a visual scene by combinatorial processing) rather than the detection of low-level stimulus features. It may be that RF nonlinearities previously described in mammalian V1 and related to stimulus or behavioral contexts (Baudot et al., 2013; David et al., 2004; Keller et al., 2012; Saleem et al., 2013) correspond to an encoding of latent variables distributed across the V1 neural population, similar to how visual space is encoded in dCx.

Selective Encoding at the Single-Cell Level

The decomposition of RFs into linear and nonlinear components showed that spatial features of a stimulus (e.g., position and orientation) may also be encoded at the single-cell level in dCx. Most linear RFs show a predominance of ON or OFF

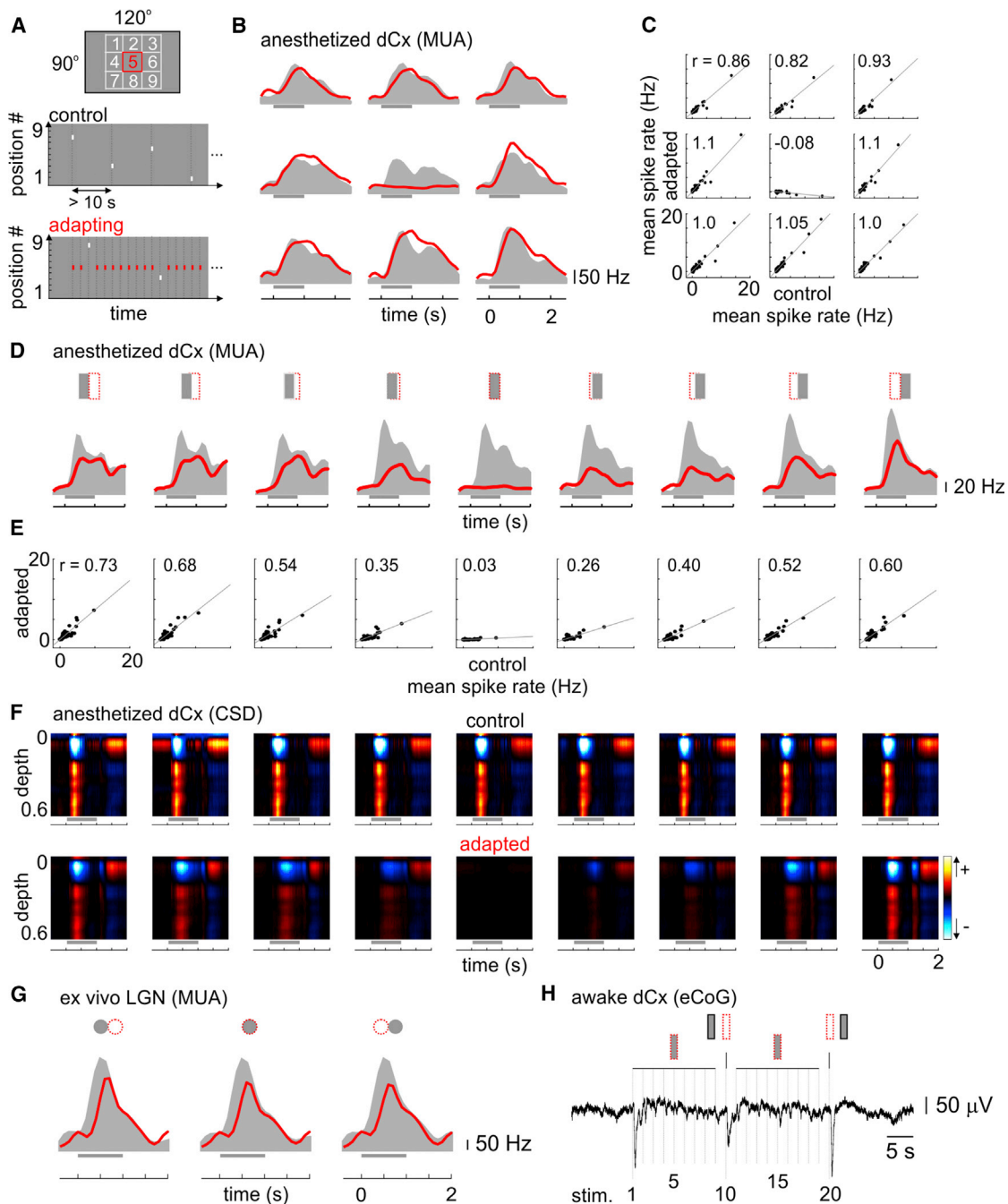


Figure 8. Spatially Selective Adaptation in dCx

(A) Example of control- and adapting-stimulation paradigms for a 3×3 stimulation grid covering $90^\circ \times 90^\circ$ of visual angle (inset at top).
 (B) Stimulus-triggered population response measured in an anesthetized animal with the control (gray) and adapting (red) stimulation. Note response suppression by adaptation in position 5.
 (C) Population comparison of the mean firing rates after stimulus onset between control (x axis) and adapting (y axis) stimulations, across all 3×3 positions. Each dot corresponds to one neuron.
 (D and E) Same procedure as in (B) and (C), except that the stimulation grid consisted of nine vertical bars (20° of visual angle each), shifted horizontally in increments corresponding to 25% of the width of the stimulus (5° of visual angle). Note progressive and proportional relationship between overlap and response.
 (F) CSD profiles measured in an anesthetized animal during the same control (top) and adapting (bottom) conditions as in (D). Depth is in mm.
 (G) Population responses recorded in LGN, *ex vivo* (STAR Methods), with control (gray) and adapting (red) stimulations using a 1×3 stimulation grid. Note absence of spatially selective adaptation.
 (H) Example of average eCoG response recorded in the awake turtle (STAR Methods). The stimulation grid consisted of three non-overlapping vertical bars. The middle one was flashed repeatedly every 2 s, except at stimuli #10 and #20, where the left bar or the right bar was flashed. See also Figure S8.

responses, but some (~35%) have adjacent ON and OFF subfields. These are reminiscent of those described in mammalian V1 simple cells, though much larger. However, the amplitudes of these selective linear RFs relative to the overall response were small, consistent with a prior suggestion that visual position might be encoded in small amplitude components of the global dCx response (Senseman and Robbins, 1999). We did not observe clearly significant linear RF components in response to sparse noise in dCx. This may be due to the fact that estimating such small components requires a great many trials, achievable only with dense stimuli. It is also possible that the relative weight of these linear RF components is much reduced in a sparse visual context, as observed in cat V1 (Fournier et al., 2011). Although the mechanisms underlying the spatial selectivity of these linear RFs probably differ from those in their mammalian counterpart, visual processing in turtle dCx might share some basic computational features with mammalian V1, reflecting common statistical constraints imposed by the visual world (Olshausen and Field, 1996).

Stimulus Specific Adaptation

Our recordings revealed a prominent degree of spatial adaptation in dCx neuron responses. This suggests that spatiotemporal correlations of input stimuli play an important role in driving dCx neurons. Repeated stimulation (at intervals <5 s; Luo et al., 2010) of an area of the visual field resulted in a selective reduction of the response of individual neurons to that stimulus location, but not to surrounding areas. This form of stimulus-specific adaptation is similar to those reported in mammalian primary sensory areas (olfactory [Best and Wilson, 2004; Wilson, 1998], auditory [Ulanovsky et al., 2003], and visual [Benucci et al., 2013; Dragoi et al., 2000; Müller et al., 1999] cortices; higher-order cortices [e.g., ITC; De Baene and Vogels, 2010; Miller et al., 1991]; superior colliculus [Boehnke et al., 2011]; and avian tectum [Reches and Gutfreund, 2008]). Therefore, dCx exhibits a property that is common to many sensory systems in amniotes. Whether or not adaptation reflects an intrinsic component of the stimulus-encoding process, it is consistent with redundancy-reduction ideas whereby neurons maximize information transfer by removing components of the sensory input that are overrepresented. Recent evidence suggests that this adaptation could also contribute to stabilizing the network in a *critical* regime, compensating for transient activations by strong sensory stimuli (Shew et al., 2015).

CSD profiles suggest that this adaptation results from a dramatic reduction of the thalamic drive to dCx. Because LGN neurons do not exhibit any spatially selective adaptation under the same stimulus conditions, we propose that this adaptation results from a selective depression of thalamocortical synapses. This mechanism is reminiscent, in the spatial domain, of what is observed in mammalian piriform cortex (PCx): odor-specific adaptation of PCx-neuron responses to repetitive stimulation results, at least in part, from a synaptic depression of lateral olfactory tract terminals with origin in the set of glomeruli that were selectively activated by the stimulating odor (Best and Wilson, 2004).

Beta Range Oscillations

The tendency of flashed visual stimuli to cause cortical oscillations was observed previously in head-fixed awake turtles and

in *ex vivo* brain preparations using extracellular recordings (Prechtl, 1994; Prechtl et al., 2000) or imaging techniques (VSD) (Prechtl et al., 1997; Senseman and Robbins, 1999). We confirmed these results both in anesthetized and in awake animals. Using depth recording electrodes in anesthetized animals, we establish a direct correlation between visually evoked beta-range field potential oscillations and the underlying neuronal activity: beta oscillations in dCx reflect the firing statistics of the dCx neuronal population. The function of these oscillations is at present unknown, but it may facilitate cortical processing by synchronizing subpopulations of neurons across distant parts of the dCx network, as proposed for mammalian cortex (for review, see Fries, 2009).

Thalamocortical and Intracortical Connectivity

Consistent with previous anatomical data (Mulligan and Ulinski, 1990), our retrograde tracing of LGN neurons from single cortical sites suggests a coarse imbalance of inputs from caudal and rostral LGN to dCx. Although thalamic neurons projecting to dCx are scattered across large parts, if not all, of LGN, the fraction of afferent projections from caudal LGN decreases progressively from rostral to caudal dCx.

It was previously suggested that this organization of thalamocortical afferents generates iso-azimuth lamellae in dCx, so that the naso-temporal axis of the visual field is retinotopically mapped along the rostro-caudal axis of dCx (Mulligan and Ulinski, 1990; Ulinski and Nautiyal, 1988). However, our electrophysiological data did not reveal any retinotopic mapping in dCx. The absence of retinotopy in dCx responses and the weakness of the spatial selectivity of its RFs may reflect the high distributivity of intracortical connections in turtle cortex (Cosans and Ulinski, 1990) (M. Hemberger, personal communication), which could overcome any bias in the LGN inputs.

Previous electrophysiological recordings and VSD imaging in reduced preparations show that stimulus-evoked activity travels across the entire dCx (Prechtl et al., 1997, 2000; Senseman and Robbins, 2002), suggesting that wave patterns might represent some features of a visual stimulus (Senseman and Robbins, 1999). Because propagating waves follow a rostro-caudal trajectory (Senseman, 1999), information from the temporal retina could plausibly be fed into caudal cortex via polysynaptic, intracortical links. Such a scenario could also underlie the extraction of positional information during prolonged responses, e.g., by the analysis of the temporal delay of direct thalamocortical and intracortical activity. A temporal separation between stimulus detection and discrimination of visual stimuli in turtle cortex has been proposed recently (Clawson et al., 2017).

Our data show that RFs are not uniform across local populations of dCx neurons. They also tend to be less similar across different parts of dCx than within a local population. This heterogeneity may result from biases in LGN input selectivity at both single-cell and subnetwork levels (e.g., with respect to the ON or OFF selectivity or the position of the LGN RFs). The fact that we observed less than 2% of double-labeled LGN cells when using different tracers along the rostro-caudal axis of dCx argues for the existence of such biases in the LGN inputs to different cortical locations. Nevertheless, the heterogeneity of dCx RFs could also reflect local connectivity biases between dCx

neurons, e.g., by convergence of inputs from dCx neurons sharing the same imbalance across their LGN inputs.

Visual Processing in Turtle Visual Cortex: Relation to Mammalian Sensory Cortices

Our results show that despite a lack of clear retinotopic mapping of visual space in dCx, spatial information about visual scenes can be retrieved by analysis of dCx neuron responses. Though present, the structure of dCx RFs appears very coarse at best, and the absence of maps makes it unlikely that RFs are optimized for detection of fine stimulus features. The optic tectum, with its fine RF structure and mapped projections (Stirling et al., 1998), probably plays that role. Support for such a functional dichotomy of the collo- and the lemno-thalamic visual pathways, present in all amniotes, comes from lesion studies showing deficits in pattern and brightness discrimination only upon destruction of the tectofugal pathway (Cranney and Powers, 1983; Reiner and Powers, 1983). Although dCx is the first stage of cortical visual processing in turtles, the distributed representations seen there suggest at least two possible forms of processing, thus far unseen in any V1.

The first is reminiscent of primary olfactory processing, in which olfactory bulb projections form widely distributed and seemingly random contacts with PCx pyramidal neurons (Ghosh et al., 2011; Miyamichi et al., 2011). In such a system, odor identity can be retrieved by decoding a distributed representation (Davison and Ehlers, 2011; Poo and Isaacson, 2009; Roland et al., 2017; Stettler and Axel, 2009). Such design may hold as long as the dimensionality of inputs is relatively limited (e.g., odor identity and intensity) and is similar to that initially described in insect olfactory circuits (Perez-Orive et al., 2002; Stopfer et al., 2003). The absence of fine mapping of thalamocortical projections to dCx and the selective adaptation of thalamic inputs to dCx are both consistent with such design similarity between olfactory and visual cortices in turtle (Fournier et al., 2015). This idea is also consistent with the hypothesis that cerebral cortex evolved first among amniotes as an associative (olfactory) structure (Aboitiz and Montiel, 2015).

The second suggested form of processing—one that is not inconsistent with the first—is reminiscent of high-order sensory areas in mammals. In this scheme, dCx might represent visual inputs by segmentation along a manifold that corresponds to high-order features of the visual scene, akin to that suggested for object recognition along the ventral stream in mammals (DiCarlo et al., 2012). dCx would thus perform a global, rather than local, analysis of visual scenes, possibly leading to the extraction of behaviorally relevant features. Lesion experiments in turtles suggested a role for medial cortex (mCx) in spatial learning and memory formation (Grisham and Powers, 1989, 1990; López et al., 2003a, 2003b). Anatomical (Striedter, 2016), developmental (Medina et al., 2013; Puelles, 2001), and single-cell transcriptomics studies (M. Tosches, T. Yamawaki, R. Naumann et al., personal communication) suggest that much of reptilian general cortex may be equivalent, if not homologous, to mammalian hippocampus. The abundant direct projections from dCx to mCx (Desan, 1985; Ulinski, 1990) support the hypothesis that computations in dCx reflect a global processing of visual scenes, similar to how space and visual features are

represented in cortical areas directly connected to the hippocampus in mammals (e.g., peri- and post-rhinal cortices [Ramos, 2013] or lateral and medial entorhinal cortices [Killian et al., 2012; Knierim et al., 2013; Moser et al., 2008; Tsao et al., 2013; Yoo and Lee, 2017]).

In conclusion, our results suggest that the organizational principles of this primitive visual cortex differ significantly from those of mammalian V1. They suggest that the fine spatial mapping of primary sensory attributes, well described in mammalian primary neocortical areas (such as V1, S1, or A1), is not an ancestral feature of amniote cortex, but rather appears only in the mammalian lineage, paralleling the expansion of cortical layering and the evolution of precisely targeted thalamocortical projections to novel and specialized layers (rather than diffuse projections to distal layer 1, as seen in turtle dCx).

STAR★METHODS

Detailed methods are provided in the online version of this paper and include the following:

- KEY RESOURCES TABLE
- CONTACT FOR REAGENT AND RESOURCE SHARING
- EXPERIMENTAL MODEL AND SUBJECT DETAILS
- METHOD DETAILS
 - Electrophysiology
 - Histology
 - Visual Stimuli
 - Time-Frequency analysis of LFP and eCoG data
 - Receptive field estimation
 - Bayesian decoding
 - Peri-Oscillation Triggered Histograms and Current Source Density analysis
- QUANTIFICATION AND STATISTICAL ANALYSIS
- DATA AND SOFTWARE AVAILABILITY

SUPPLEMENTAL INFORMATION

Supplemental Information includes eight figures and can be found with this article online at <https://doi.org/10.1016/j.neuron.2017.11.017>.

ACKNOWLEDGMENTS

We are indebted to Michaela Klinkmann and Anja Arends for help with surgery and histology, to the members of the Laurent lab for discussion, and to the reviewers for many helpful comments. We also thank Yves Fregnac and Aman Saleem for helpful discussions. Funding was provided by the Max Planck Society, the European Research Council under the European Union's Seventh Framework Programme (FP7/2007-2013)/ERC grant agreement no. 322705 (G.L.), and the Human Frontier Science Program (J.F.).

AUTHOR CONTRIBUTIONS

Conceptualization, J.F., C.M.M., and G.L.; Methodology, all authors; Investigation: J.F., C.M.M., and I.S.; Formal Analysis, J.F. and C.M.M.; Writing – Original Draft, J.F., C.M.M., and G.L.; Writing – Review & Editing, all authors.

Received: April 24, 2017

Revised: August 25, 2017

Accepted: November 10, 2017

Published: December 14, 2017

REFERENCES

- Aboitiz, F., and Montiel, J.F. (2015). Olfaction, navigation, and the origin of iso-cortex. *Front. Neurosci.* 9, 402.
- Baudot, P., Levy, M., Marre, O., Monier, C., Pananceau, M., and Frégnac, Y. (2013). Animation of natural scene by virtual eye-movements evokes high precision and low noise in V1 neurons. *Front. Neural Circuits* 7, 206.
- Bendor, D., and Wilson, M.A. (2012). Biasing the content of hippocampal replay during sleep. *Nat. Neurosci.* 15, 1439–1444.
- Benucci, A., Saleem, A.B., and Carandini, M. (2013). Adaptation maintains population homeostasis in primary visual cortex. *Nat. Neurosci.* 16, 724–729.
- Best, A.R., and Wilson, D.A. (2004). Coordinate synaptic mechanisms contributing to olfactory cortical adaptation. *J. Neurosci.* 24, 652–660.
- Boehnke, S.E., Berg, D.J., Marino, R.A., Baldi, P.F., Itti, L., and Munoz, D.P. (2011). Visual adaptation and novelty responses in the superior colliculus. *Eur. J. Neurosci.* 34, 766–779.
- Bolding, K.A., and Franks, K.M. (2017). Complementary codes for odor identity and intensity in olfactory cortex. *eLife* 6, <https://doi.org/10.7554/eLife.22630>.
- Brown, K.T. (1969). A linear area centralis extending across the turtle retina and stabilized to the horizon by non-visual cues. *Vision Res.* 9, 1053–1062.
- Butler, A.B., Reiner, A., and Karten, H.J. (2011). Evolution of the amniote pallium and the origins of mammalian neocortex. *Ann. N.Y. Acad. Sci.* 1225, 14–27.
- Clawson, W.P., Wright, N.C., Wessel, R., and Shew, W.L. (2017). Adaptation towards scale-free dynamics improves cortical stimulus discrimination at the cost of reduced detection. *PLoS Comput. Biol.* 13, e1005574.
- Cosans, C.E., and Ulinski, P.S. (1990). Spatial organization of axons in turtle visual cortex: intralamellar and interlamellar projections. *J. Comp. Neurol.* 296, 548–558.
- Cranney, J., and Powers, A.S. (1983). The effects of core nucleus and cortical lesions in turtles on reversal and dimensional shifting. *Physiol. Psychol.* 11, 103–111.
- David, S.V., Vinje, W.E., and Gallant, J.L. (2004). Natural stimulus statistics alter the receptive field structure of V1 neurons. *J. Neurosci.* 24, 6991–7006.
- Davison, I.G., and Ehlers, M.D. (2011). Neural circuit mechanisms for pattern detection and feature combination in olfactory cortex. *Neuron* 70, 82–94.
- De Baene, W., and Vogels, R. (2010). Effects of adaptation on the stimulus selectivity of macaque inferior temporal spiking activity and local field potentials. *Cereb. Cortex* 20, 2145–2165.
- DeAngelis, G.C., Ohzawa, I., and Freeman, R.D. (1993). Spatiotemporal organization of simple-cell receptive fields in the cat's striate cortex. I. General characteristics and postnatal development. *J. Neurophysiol.* 69, 1091–1117.
- Desan, P.H. (1984). The Organization of the Cerebral Cortex of the Pond Turtle, *Pseudemys scripta elegans* (Harvard University).
- Desan, P.H. (1985). Organization of the cerebral cortex in turtle. In *The Forebrain of Reptiles*, W.K. Schwerdtfeger and W.J. Smeets, eds. (Karger), pp. 1–11.
- Desimone, R., Albright, T.D., Gross, C.G., and Bruce, C. (1984). Stimulus-selective properties of inferior temporal neurons in the macaque. *J. Neurosci.* 4, 2051–2062.
- DiCarlo, J.J., Zoccolan, D., and Rust, N.C. (2012). How does the brain solve visual object recognition? *Neuron* 73, 415–434.
- Dragoi, V., Sharma, J., and Sur, M. (2000). Adaptation-induced plasticity of orientation tuning in adult visual cortex. *Neuron* 28, 287–298.
- Emerson, R.C., Citron, M.C., Vaughn, W.J., and Klein, S.A. (1987). Nonlinear directionally selective subunits in complex cells of cat striate cortex. *J. Neurophysiol.* 58, 33–65.
- Fournier, J., Monier, C., Pananceau, M., and Frégnac, Y. (2011). Adaptation of the simple or complex nature of V1 receptive fields to visual statistics. *Nat. Neurosci.* 14, 1053–1060.
- Fournier, J., Monier, C., Levy, M., Marre, O., Sári, K., Kisvárdy, Z.F., and Frégnac, Y. (2014). Hidden complexity of synaptic receptive fields in cat V1. *J. Neurosci.* 34, 5515–5528.
- Fournier, J., Müller, C.M., and Laurent, G. (2015). Looking for the roots of cortical sensory computation in three-layered cortices. *Curr. Opin. Neurobiol.* 31, 119–126.
- Fournier, J., Mueller, C.M., Shein-Idelson, M., Hemberger, M., and Laurent, G. (2016). Consensus-based sorting of neuronal spike waveforms. *PLoS ONE* 11, e0160494.
- Fries, P. (2009). Neuronal gamma-band synchronization as a fundamental process in cortical computation. *Annu. Rev. Neurosci.* 32, 209–224.
- Ghosh, S., Larson, S.D., Hefzi, H., Marnoy, Z., Cutforth, T., Dokka, K., and Baldwin, K.K. (2011). Sensory maps in the olfactory cortex defined by long-range viral tracing of single neurons. *Nature* 472, 217–220.
- Glickstein, M., and Millodot, M. (1970). Retinoscopy and eye size. *Science* 168, 605–606.
- Graf, V. (1967). A spectral sensitivity curve and wavelength discrimination for the turtle *Chrysemys picta picta*. *Vision Res.* 7, 915–928.
- Grisham, W., and Powers, A.S. (1989). Function of the dorsal and medial cortex of turtles in learning. *Behav. Neurosci.* 103, 991–997.
- Grisham, W., and Powers, A.S. (1990). Effects of dorsal and medial cortex lesions on reversals in turtles. *Physiol. Behav.* 47, 43–49.
- Gusel'nikov, V.I., and Pivovarov, A.S. (1978). Postsynaptic mechanism of habituation of turtle cortical neurons to moving stimuli. *Neurosci. Behav. Physiol.* 9, 1–7.
- Gusel'nikov, V.I., Morenkov, E.D., and Pivovarov, A.S. (1972). Unit responses of the turtle forebrain to visual stimuli. *Neurosci. Behav. Physiol.* 5, 235–242.
- Hall, W.C., and Ebner, F.F. (1970). Thalamotellencephalic projections in the turtle (*Pseudemys scripta*). *J. Comp. Neurol.* 140, 101–122.
- Hall, J.A., Foster, R.E., Ebner, F.F., and Hall, W.C. (1977). Visual cortex in a reptile, the turtle (*Pseudemys scripta* and *Chrysemys picta*). *Brain Res.* 130, 197–216.
- Hastie, T.J., Tibshirani, R.J., and Friedman, J.H. (2009). *The Elements of Statistical Learning: Data Mining, Inference, and Prediction* (Springer).
- Hayes, W.N., Hertzler, D.R., and Hogberg, D.K. (1968). Visual responsiveness and habituation in the turtle. *J. Comp. Physiol. Psychol.* 65, 331–335.
- Heller, S.B., and Ulinski, P.S. (1987). Morphology of geniculocortical axons in turtles of the genera *Pseudemys* and *Chrysemys*. *Anat. Embryol. (Berl.)* 175, 505–515.
- Hubel, D.H., and Wiesel, T.N. (1962). Receptive fields, binocular interaction and functional architecture in the cat's visual cortex. *J. Physiol.* 160, 106–154.
- Hung, C.P., Kreiman, G., Poggio, T., and DiCarlo, J.J. (2005). Fast readout of object identity from macaque inferior temporal cortex. *Science* 310, 863–866.
- Keller, G.B., Bonhoeffer, T., and Hübner, M. (2012). Sensorimotor mismatch signals in primary visual cortex of the behaving mouse. *Neuron* 74, 809–815.
- Kiani, R., Esteky, H., Mirpour, K., and Tanaka, K. (2007). Object category structure in response patterns of neuronal population in monkey inferior temporal cortex. *J. Neurophysiol.* 97, 4296–4309.
- Killian, N.J., Jutras, M.J., and Buffalo, E.A. (2012). A map of visual space in the primate entorhinal cortex. *Nature* 491, 761–764.
- Knierim, J.J., Neunuebel, J.P., and Deshmukh, S.S. (2013). Functional correlates of the lateral and medial entorhinal cortex: objects, path integration and local-global reference frames. *Philos. Trans. R. Soc. Lond. B Biol. Sci.* 369, 20130369.
- Levy, M., Fournier, J., and Frégnac, Y. (2013). The role of delayed suppression in slow and fast contrast adaptation in V1 simple cells. *J. Neurosci.* 33, 6388–6400.
- Lien, A.D., and Scanziani, M. (2013). Tuned thalamic excitation is amplified by visual cortical circuits. *Nat. Neurosci.* 16, 1315–1323.
- López, J.C., Vargas, J.P., Gómez, Y., and Salas, C. (2003a). Spatial and non-spatial learning in turtles: the role of medial cortex. *Behav. Brain Res.* 143, 109–120.
- López, J.C., Gómez, Y., Vargas, J.P., and Salas, C. (2003b). Spatial reversal learning deficit after medial cortex lesion in turtles. *Neurosci. Lett.* 341, 197–200.

- Luo, Q., Lu, H., Lu, H., Yang, Y., and Gao, J.H. (2010). Comparison of visually evoked local field potentials in isolated turtle brain: patterned versus blank stimulation. *J. Neurosci. Methods* 187, 26–32.
- Machens, C.K., Wehr, M.S., and Zador, A.M. (2004). Linearity of cortical receptive fields measured with natural sounds. *J. Neurosci.* 24, 1089–1100.
- Marfurt, C.F., Turner, D.F., and Adams, C.E. (1988). Stabilization of tetramethylbenzidine (TMB) reaction product at the electron microscopic level by ammonium molybdate. *J. Neurosci. Methods* 25, 215–223.
- Marshall, J.H., Garrett, M.E., Nauhaus, I., and Callaway, E.M. (2011). Functional specialization of seven mouse visual cortical areas. *Neuron* 72, 1040–1054.
- Mazurskaya, P.Z. (1973). Organization of receptive fields in the forebrain of *Emys orbicularis*. *Neurosci. Behav. Physiol.* 6, 311–318.
- Mazurskaya, P.Z., Davydova, T.V., and Smirnov, G.D. (1967). Functional organization of exteroceptive projections in the forebrain of the turtle. *Neurosci. Behav. Physiol.* 1, 109–117.
- Medina, L., Abellán, A., and Desfilis, E. (2013). A never-ending search for the evolutionary origin of the neocortex: rethinking the homology concept. *Brain Behav. Evol.* 81, 150–153.
- Mesulam, M.M. (1978). Tetramethyl benzidine for horseradish peroxidase neurohistochemistry: a non-carcinogenic blue reaction product with superior sensitivity for visualizing neural afferents and efferents. *J. Histochem. Cytochem.* 26, 106–117.
- Miller, E.K., Li, L., and Desimone, R. (1991). A neural mechanism for working and recognition memory in inferior temporal cortex. *Science* 254, 1377–1379.
- Miura, K., Mainen, Z.F., and Uchida, N. (2012). Odor representations in olfactory cortex: distributed rate coding and decorrelated population activity. *Neuron* 74, 1087–1098.
- Miyamichi, K., Amat, F., Moussavi, F., Wang, C., Wickersham, I., Wall, N.R., Taniguchi, H., Tasic, B., Huang, Z.J., He, Z., et al. (2011). Cortical representations of olfactory input by trans-synaptic tracing. *Nature* 472, 191–196.
- Mori, K., Nowicky, M.C., and Shepherd, G.M. (1981). Electrophysiological analysis of mitral cells in the isolated turtle olfactory bulb. *J. Physiol.* 314, 281–294.
- Morlock, H.C. (1972). Behavior following ablation of the dorsal cortex of turtles. *Brain Behav. Evol.* 5, 256–272.
- Moser, E.I., Kropff, E., and Moser, M.-B. (2008). Place cells, grid cells, and the brain's spatial representation system. *Annu. Rev. Neurosci.* 31, 69–89.
- Movshon, J.A., Thompson, I.D., and Tolhurst, D.J. (1978). Receptive field organization of complex cells in the cat's striate cortex. *J. Physiol.* 283, 79–99.
- Müller, J.R., Metha, A.B., Krauskopf, J., and Lennie, P. (1999). Rapid adaptation in visual cortex to the structure of images. *Science* 285, 1405–1408.
- Mulligan, K.A., and Ulinski, P.S. (1990). Organization of geniculocortical projections in turtles: isoazimuth lamellae in the visual cortex. *J. Comp. Neurol.* 296, 531–547.
- Nahmani, M., and Erisir, A. (2005). VGluT2 immunocytochemistry identifies thalamocortical terminals in layer 4 of adult and developing visual cortex. *J. Comp. Neurol.* 484, 458–473.
- Northmore, D.P., and Granda, A.M. (1991). Refractive state, contrast sensitivity, and resolution in the freshwater turtle, *Pseudemys scripta elegans*, determined by tectal visual-evoked potentials. *Vis. Neurosci.* 7, 619–625.
- Olshausen, B.A., and Field, D.J. (1996). Emergence of simple-cell receptive field properties by learning a sparse code for natural images. *Nature* 381, 607–609.
- Perez-Orive, J., Mazor, O., Turner, G.C., Cassenaer, S., Wilson, R.I., and Laurent, G. (2002). Oscillations and sparsening of odor representations in the mushroom body. *Science* 297, 359–365.
- Peterson, E.H., and Ulinski, P.S. (1979). Quantitative studies of retinal ganglion cells in a turtle, *Pseudemys scripta elegans*. I. Number and distribution of ganglion cells. *J. Comp. Neurol.* 186, 17–42.
- Pettersen, K.H., Devor, A., Ulbert, I., Dale, A.M., and Einevoll, G.T. (2006). Current-source density estimation based on inversion of electrostatic forward solution: effects of finite extent of neuronal activity and conductivity discontinuities. *J. Neurosci. Methods* 154, 116–133.
- Poo, C., and Isaacson, J.S. (2009). Odor representations in olfactory cortex: “sparse” coding, global inhibition, and oscillations. *Neuron* 62, 850–861.
- Powers, A.S., and Reiner, A. (1980). A stereotaxic atlas of the forebrain and midbrain of the eastern painted turtle (*Chrysemys picta picta*). *J. Hirnforsch.* 21, 125–159.
- Prechtl, J.C. (1994). Visual motion induces synchronous oscillations in turtle visual cortex. *Proc. Natl. Acad. Sci. USA* 91, 12467–12471.
- Prechtl, J.C., Cohen, L.B., Pesaran, B., Mitra, P.P., and Kleinfeld, D. (1997). Visual stimuli induce waves of electrical activity in turtle cortex. *Proc. Natl. Acad. Sci. USA* 94, 7621–7626.
- Prechtl, J.C., Bullock, T.H., and Kleinfeld, D. (2000). Direct evidence for local oscillatory current sources and intracortical phase gradients in turtle visual cortex. *Proc. Natl. Acad. Sci. USA* 97, 877–882.
- Puelles, L. (2001). Thoughts on the development, structure and evolution of the mammalian and avian telencephalic pallium. *Philos. Trans. R. Soc. Lond. B Biol. Sci.* 356, 1583–1598.
- Quiñero, R., and Panzeri, S. (2009). Extracting information from neuronal populations: information theory and decoding approaches. *Nat. Rev. Neurosci.* 10, 173–185.
- Ramos, J.M.J. (2013). Differential contribution of hippocampus, perirhinal cortex and postrhinal cortex to allocentric spatial memory in the radial maze. *Behav. Brain Res.* 247, 59–64.
- Reches, A., and Gutfreund, Y. (2008). Stimulus-specific adaptations in the gaze control system of the barn owl. *J. Neurosci.* 28, 1523–1533.
- Reiner, A. (1991). A comparison of neurotransmitter-specific and neuropeptide-specific neuronal cell types present in the dorsal cortex in turtles with those present in the isocortex in mammals: implications for the evolution of isocortex. *Brain Behav. Evol.* 38, 53–91.
- Reiner, A., and Powers, A.S. (1983). The effects of lesions of telencephalic visual structures on visual discriminative performance in turtles (*Chrysemys picta picta*). *J. Comp. Neurol.* 218, 1–24.
- Roland, B., Deneux, T., Franks, K.M., Bathellier, B., and Fleischmann, A. (2017). Odor identity coding by distributed ensembles of neurons in the mouse olfactory cortex. *eLife* 6, <https://doi.org/10.7554/eLife.26337>.
- Rust, N.C., Schwartz, O., Movshon, J.A., and Simoncelli, E.P. (2005). Spatiotemporal elements of macaque V1 receptive fields. *Neuron* 46, 945–956.
- Rutishauser, U., Kotowicz, A., and Laurent, G. (2013). A method for closed-loop presentation of sensory stimuli conditional on the internal brain-state of awake animals. *J. Neurosci. Methods* 215, 139–155.
- Saleem, A.B., Ayaz, A., Jeffery, K.J., Harris, K.D., and Carandini, M. (2013). Integration of visual motion and locomotion in mouse visual cortex. *Nat. Neurosci.* 16, 1864–1869.
- Senseman, D.M. (1996). Correspondence between visually evoked voltage-sensitive dye signals and synaptic activity recorded in cortical pyramidal cells with intracellular microelectrodes. *Vis. Neurosci.* 13, 963–977.
- Senseman, D.M. (1999). Spatiotemporal structure of depolarization spread in cortical pyramidal cell populations evoked by diffuse retinal light flashes. *Vis. Neurosci.* 16, 65–79.
- Senseman, D.M., and Robbins, K.A. (1999). Modal behavior of cortical neural networks during visual processing. *J. Neurosci.* 19, RC3.
- Senseman, D.M., and Robbins, K.A. (2002). High-speed VSD imaging of visually evoked cortical waves: decomposition into intra- and intercortical wave motions. *J. Neurophysiol.* 87, 1499–1514.
- Shew, W.L., Clawson, W.P., Pobst, J., Karimipour, Y., Wright, N.C., and Wessel, R. (2015). Adaptation to sensory input tunes visual cortex to criticality. *Nat. Phys.* 11, 659–663.
- Stettler, D.D., and Axel, R. (2009). Representations of odor in the piriform cortex. *Neuron* 63, 854–864.

- Stirling, R.V., Dunlop, S.A., and Beazley, L.D. (1998). An in vitro technique for electrophysiological mapping of reptilian retinotectal projections. *J. Neurosci. Methods* 87, 85–89.
- Stopfer, M., Jayaraman, V., and Laurent, G. (2003). Intensity versus identity coding in an olfactory system. *Neuron* 39, 991–1004.
- Striedter, G.F. (2016). Evolution of the hippocampus in reptiles and birds. *J. Comp. Neurol.* 524, 496–517.
- Touryan, J., Felsen, G., and Dan, Y. (2005). Spatial structure of complex cell receptive fields measured with natural images. *Neuron* 45, 781–791.
- Tsao, A., Moser, M.B., and Moser, E.I. (2013). Traces of experience in the lateral entorhinal cortex. *Curr. Biol.* 23, 399–405.
- Ulanovsky, N., Las, L., and Nelken, I. (2003). Processing of low-probability sounds by cortical neurons. *Nat. Neurosci.* 6, 391–398.
- Ulinski, P.S. (1990). The cerebral cortex of reptiles. *Cereb. Cortex* 8A, 139–216.
- Ulinski, P.S., and Nautiyal, J. (1988). Organization of retinogeniculate projections in turtles of the genera *Pseudemys* and *Chrysemys*. *J. Comp. Neurol.* 276, 92–112.
- Wichmann, F.A., Braun, D.I., and Gegenfurtner, K.R. (2006). Phase noise and the classification of natural images. *Vision Res.* 46, 1520–1529.
- Wilson, D.A. (1998). Habituation of odor responses in the rat anterior piriform cortex. *J. Neurophysiol.* 79, 1425–1440.
- Yoo, S., and Lee, I. (2017). Functional double dissociation within the entorhinal cortex for visual scene-dependent choice behavior. *eLife* 6, <https://doi.org/10.7554/eLife.21543>.
- Zhang, K., Ginzburg, I., McNaughton, B.L., and Sejnowski, T.J. (1998). Interpreting neuronal population activity by reconstruction: unified framework with application to hippocampal place cells. *J. Neurophysiol.* 79, 1017–1044.
- Zhu, D., Lustig, K.H., Bifulco, K., and Keifer, J. (2005). Thalamocortical connections in the pond turtle *Pseudemys scripta elegans*. *Brain Behav. Evol.* 65, 278–292.

STAR★METHODS

KEY RESOURCES TABLE

REAGENT or RESOURCE	SOURCE	IDENTIFIER
Antibodies		
NeuN (clone A60), mouse monoclonal (1:500 to 1:2000)	Millipore	Cat# MAB377; RRID: AB_2298772
vGluT2, rabbit polyclonal (1:500 to 1:3000)	Synaptic Systems	Cat# 135 403; RRID: AB_887883
Donkey-anti-mouse-Alexa(488 or 568)	Thermo Fisher Scientific	Cat# A-21202; RRID: AB_141607; Cat# A-10037; RRID: AB_2534013
Donkey-anti-rabbit-Alexa(488 or 568)	Thermo Fisher Scientific	Cat# A-21206; RRID: AB_2535792; Cat# A-10042; RRID: AB_2534017
Chemicals, Peptides, and Recombinant Proteins		
Ketamine (100mg/ml)	Cp-Pharma	https://www.cp-pharma.de/
Dexdomitor (dexmedetomidine)	Vétoquinol GmbH	http://www.vetoquinol.de/
Isoflurane	Baxter	http://www.baxter.de/index.page
Rimadyl (carprofene), analgetic	Cp-Pharma	https://www.cp-pharma.de/
Other chemicals (all research grade)	Sigma	https://www.sigmaaldrich.com/
Experimental Models: Organisms/Strains		
<i>Trachemys scripta</i> sp. (red-eared slider turtles)	Nasco	https://www.enasco.com/
Software and Algorithms		
MATLAB (versions 2015b to 2017a)	MathWorks	RRID: SCR_001622
ImageJ 1.51p	N/A	RRID: SCR_003070
Consensus-Based Sorting of Neuronal Spike Waveforms	Fournier et al., 2016	N/A
Cheetah Data Acquisition Software	https://neuralynx.com/research_software/data_acquisition_software/	N/A
Other		
Neuronexus electrodes	http://neuronexus.com	N/A
Neuralynx	https://neuralynx.com/products/digital_data_acquisition_systems/	Digital Lynx 16SX
Viewpixmap Monitor	http://vpixx.com/	VIEWPixmap /3D, RRID: SCR_009646
PROPixx DLP projector	http://vpixx.com/	PROPixx, RRID: SCR_013299
Animal respirator, Inspira ASVv	Harvard Apparatus	https://www.hugo-sachs.de/index.php/
Capnograph Type 340	Harvard Apparatus	https://www.hugo-sachs.de/index.php/
Vapor 19.3 (Isoflurane)	Eickenmeyer Dräger	http://www.eickemeyer.de/#S11957
Image-Collection	McGill image database	http://tabby.vision.mcgill.ca/html/browsedownload.html
Turtle movies	ReefVid free video clips	http://www.reefvid.org/

CONTACT FOR REAGENT AND RESOURCE SHARING

Further information and requests for reagents may be directed to and will be fulfilled by the Lead Contact, Gilles Laurent (gilles.laurent@brain.mpg.de).

EXPERIMENTAL MODEL AND SUBJECT DETAILS

Data presented here were collected from adult turtles (*Trachemys scripta scripta*, $n = 15$) of either sex. Animals were housed in groups of 2 or 3 animals in water tanks. Chronically implanted animals ($n = 4$) were housed individually after implantation and brought for repeated recording session over a period of up to 4 weeks. All experimental procedures followed institutional guidelines and were approved by the local authorities (RP Darmstadt, protocol F122/13).

METHOD DETAILS

Depending on experimental needs and technical feasibility, imposed by the anatomy (head-neck musculature, large subdural space, large ventricles) and behavior (head retraction) of turtles, we used several experimental techniques described in the following. The electrophysiological techniques include: 1) Local field recordings in awake animals with chronically implanted planar electrode arrays; 2) extracellular single- and multi-unit recordings in lightly anesthetized and paralyzed turtles; and 3) extracellular recordings from thalamus in an eye-brain explant preparation (*ex vivo*). Anatomical techniques include: 1) *trans*-synaptic tracing from the eye to cortex; 2) reconstruction of recording sites; 3) immunocytochemistry to define cortical layers and brain architecture; and 4) retrograde tracing from recording sites to LGN.

A general outline of the position of turtle visual cortex is shown in Figure 1A. Turtle dorsal cortex extends over each hemisphere of the dorsal telencephalon. It is posterior to the olfactory bulb and flanked laterally by the olfactory or lateral cortex (ICx); the apparent boundary between ICx and dCx follows the rhinal fissure, which can be detected superficially as a shallow dorsal indentation of the dorsal cortex running at a slight angle from the parasagittal plane (rf; Figures 1A and 1E). The rhinal fissure lies over what is known as the pallial thickening (PT; Figure 1A), a folded plate of cortex located below ICx and dCx. In transverse sections, the PT cell layer curves dorso-medially and flattens out to run in a tangential plane parallel to the pia (Figure 1A). This flattening out represents the transition to dCx, which receives direct projections from the lateral geniculate nucleus (LGN). LGN axons run all the way from thalamus down via the lateral forebrain bundle ventrally, through and around the striatum before running upward through PT, terminating in dCx, after entering it laterally. Medial to dCx are the dorso-medial (dmCx) and medial (mCx) cortices (Figure 1A), often lumped into a cortex described as “hippocampus.”

Electrophysiology

Awake eCoG recordings

Electrocorticograms (eCoGs) of visual responses were performed in 4 awake turtles using 64-channel surface electrodes (Neuronexus), placed subdurally over the dorsal cortex under deep anesthesia. After recovery from surgery, the animals could be brought for repeated awake recording sessions. Using Velcro, the turtle was fixed, plastron down, on a small horizontal plate held by a vertical pole, such that the animal's legs “floated” in air. The so-tethered animal was then placed such that its head lay at the center of a 80cm-diameter hemispherical screen (i.e., at the center of the sphere defined by the hemispherical screen). Visual stimuli were back-projected on this screen with a 60Hz LCoS-projector (liquid crystal on silicone; Canon, Ota, Tokio, Japan) after pre-warping the image to compensate for distortion on the spherical surface. Head position and movements were monitored using two infrared cameras placed at right angle, enabling 3D tracking of infrared LEDs placed on the head-mounted connector. All data were acquired with a Neuralynx amplifier.

Anesthetized recordings

The electrophysiological single unit recordings presented here were obtained from 9 adult turtles of either sex (*Trachemys scripta scripta*, 800–1500 g). We recorded from the dorsal cortex of lightly anesthetized (isoflurane, 0.5%) and paralyzed (pancuronium bromide, 0.1 ml/kg/h) animals with 32-channel linear silicon probes (20- μ m pitch, 172 μ m² surface area/site, Neuronexus) spanning 620 μ m. Prior to the experiment, we performed a craniotomy under deep anesthesia (10 mg/kg ketamine; 0.15 mg/kg dexmedetomidine I.M., maintained with 1%–3% isoflurane during artificial respiration) and implanted a metal post on the skull to stabilize the head during recording sessions that lasted up to 8 days. After infiltration of all skin wounds with local anesthetic, paralysis was initiated and maintained by I.V. and the volatile anesthetic (0.5% isoflurane) delivered by artificial ventilation (8–10 ml, 6–8 strokes/min to maintain physiological CO₂ in the exhaled air). Animals were kept on a heating pad (32°C) and their electrocardiogram monitored continuously. The eyes were covered by a thin, transparent film of 5% methylcellulose dissolved in physiological saline to prevent corneal desiccation. Eyes were inspected at regular intervals using a retinoscope, and rinsed with saline when necessary. Visual stimuli were presented to one eye on a gamma-corrected monitor (Viewpixx, 50 cm x 30 cm, 120 Hz refresh rate) with a background luminance of 12 cd.cm⁻². The screen was centered relative to the stimulated eye at a 15-cm distance from the eye. Control experiments showed that no eye correction was required, as expected from the fact that turtle eyes are emmetropic upon paralysis (Northmore and Granda, 1991) and the large depth of field of small eyes (Glickstein and Millodot, 1970). Broadband signals were recorded using a Neuralynx amplifier and digitally filtered offline between 0.2 and 4 kHz to detect spiking activity by threshold crossing. Detected events were sorted automatically using a consensus-based clustering method (Fournier et al., 2016). For population analysis, we considered only spike clusters that had an estimated fraction of misclassified spikes < 0.3, a signal-to-noise ratio > 4 and a fraction of refractory-period violations < 0.01. We identified 1000 clusters (out of 35 recording sessions), among which 350 were considered to be well isolated (fraction of misclassified spikes < 15%). All examples presented in this paper correspond to well-isolated units. For statistical population analysis, we included all the sorted units.

Ex vivo recordings

Visual responses in the lateral geniculate nucleus (LGN) were recorded *ex vivo* in an eye-brain explant preparation (n = 2 animals). Young turtles (*Trachemys scripta*, 150 to 300 g) were deeply anesthetized with ketamine (10 mg/kg, i.m.) and dexmedetomidine (Dexdomitor, 0.15 mg/kg, i.m.) and decapitated. The brain was removed in ice-cold Ringer with the eye and the optic nerves still attached

and transferred to a recording chamber perfused with an oxygenated Ringer solution (96.5 mM NaCl, 2.6 mM KCl, 4mM CaCl₂, 2 mM MgCl₂, 31.5 mM NaHCO₃, and 10 mM D-glucose, gassed to pH 7.6 with 95% O₂ and 5% CO₂; Mori et al., 1981; Senseman, 1996). The ocular globe was hemisected so as to excise the lens and expose the retina. The retina was exposed to a photostimulator, projecting the image of a gamma corrected monitor on one retinal surface. Visual responses were recorded from the contralateral LGN with 32-channel linear silicon probes (Neuronexus, see above) using a Neuralynx amplifier. LGN was targeted by inserting the electrode from the midline with a ~30° angle in direction of the optic tract. The LGN was then localized electrophysiologically by detection of a visually-evoked current sink with a slightly shorter latency than visual responses recorded in the superficial layers of the tectum.

Histology

Recording electrodes (silicon probes and surface eCoG arrays) were coated with lipophilic dyes (DiI or DiD, Molecular Probes) before implantation to mark electrode position and to define the location of thalamic afferents to recording locations by visualizing retrogradely labeled cells. After an eCoG experiment, the animal was perfused with paraformaldehyde, the brain removed and photographed under fluorescent illumination with a binocular dissection microscope to map the placement of the recording grid. After an anesthetized recording experiment, the animal was perfused with paraformaldehyde, the brain extracted and sectioned (70 µm, coronal plane). Sections were stained for NeuN, VGluT2 and DAPI and imaged under a confocal microscope. LGN cells that were retrogradely labeled from dCx recording sites were counted on every second section. The density of labeled LGN cells was expressed relative to the maximum number of cells counted across all LGN sections from the same experiment. The relative density of LGN cells along the rostro-caudal axis of LGN was aligned to the position corresponding to maximum nucleus rotundus diameter—unlike LGN, nucleus rotundus is clearly delineated, providing a reliable positional reference. For trans-neuronal tracing the plant lectin wheat germ-agglutinin coupled to horseradish peroxidase (WGA-HRP, Sigma, 1.5–2 µl of a 10% solution in PBS) was injected intra-vitreously in one eye under deep anesthesia. After a survival time of 7–8 weeks, animals were perfused with 4% paraformaldehyde/2% glutardialdehyde. Brains were extracted, soaked in 30% sucrose (in PBS) overnight, and cut with a cryotome at 60 µm. WGA-HRP was visualized according to the tetramethyl benzidine (TMB) protocol of Mesulam (1978) with subsequent stabilization of the reaction product using ammonium heptamolybdate (Marfurt et al., 1988). The distribution of TMB reaction product was documented using cross-polarized illumination. Photographs were taken with a CCD-camera mounted on a Zeiss microscope, with a 10x objective.

Visual Stimuli

Awake animals

Still images. Four categories of 2 s long stimuli covering 55° x 70° of the frontal visual field were used and presented in a fully randomized manner within each recording day:

- (1) Natural image stimuli consisted of 60 different images (selected from the McGill image database, <http://tabby.vision.mcgill.ca/html/browsedownload.html>). The images were to equal parts selected such as they represented (1) animals, (2) landscapes (land or water) or (3) man-made scenes. These images were presented in color and gray-scale.
- (2) For each of the 120 (RGB + gray scale) natural images, a phase-scrambled counterpart was generated: a uniform, random phase noise (+/– 180 degrees) was added to the complex phase component of the Fourier transform of each image; the inverse transform of this Fourier spectrum resulted in a phase-scrambled image with a frequency content matching that of the original image (Wichmann et al., 2006).
- (3) Two-dimensional white noise images (WN) with the same average pixel intensities as the natural images (RGB and gray-scale) were used as control stimuli (no intrinsic spatial correlations and flat power spectra).
- (4) Red uniform stimuli with the same dimension as the natural images were also presented. Red was chosen because the turtle retina has a high density of red cones and the behavioral spectral sensitivity is highest in the red (Graf, 1967).

All natural and control stimuli were adjusted based on their red, green and blue content to have an average luminance within ± 5% of the luminance of the gray background at the position of the turtle head in the setup.

Movies. Four 10 s-long natural movie sequences covering 30° x 60° of the frontal visual field were used for stimulation (20 fps):

- (1) *Nat*: A video file containing footage of a natural pond environment was obtained from <https://www.youtube.com/> (<https://youtu.be/07rt2ao3Yrg>), cut into 10 s clips and size adjusted. Video clips were presented both in RGB and gray-scale.
- (2) *Scr*: The same video clips (RGB and gray-scale) were presented after each frame had been phase-scrambled, to disrupt the spatial coherence.
- (3) *Shf*: The frames of the original video clips were presented in randomized order.
- (4) *Scr/Shf*: Video clips combining *Scr* and *Shf* as in 2) and 3) above.

The first frame of each movie was displayed for 2 s before the movie started, to distinguish the response to image onset from that to movie onset.

Anesthetized animals

Four types of visual stimuli were used.

- (1) “Natural movie” stimuli consisted of two successive presentations of the same movie at 20 or 25 fps (obtained from <http://www.reefvid.org>), followed by a 15 s blank period. The first frame of passage 1 of the movie was displayed for 2 s before the movie started, to distinguish the response to a flashed image from that to movie onset. All movie frames were equalized for total luminance (matching the luminance of the background) and contrast (0.9). The stimuli were presented in randomized order over each of 3×3 locations on the screen, covering $\sim 90^\circ \times 100^\circ$ of visual angle.
- (2) “Sparse noise” stimuli consisted of bright or dark non-overlapping squares (covering $90^\circ \times 120^\circ$ of visual angle; contrast = +1 or -1 on a gray background) presented sequentially over 3×5 different, randomly chosen locations on the screen for 1 s at $T > 10$ s interval.
- (3) “Dense noise” stimuli consisted of 3×5 , 4×5 or 8×10 checkerboards, covering $90^\circ \times 120^\circ$ of visual angle. The contrast value chosen for each position of the checkerboard was drawn from a uniform distribution and could either be -1, 0 or 1. Each frame of dense noise was displayed for 10 s before switching to the next frame.
- (4) “Adapting sequences” contained stimuli in 3 to 9 different possible positions (3×3 , 1×9 or 1×3), of which one (the “adapting position”) was stimulated more often than the others (“test positions”) following a randomized protocol (e.g., $P(\text{adapting}) = 0.9$; $P(\text{test}) = 0.1$). Stimuli were presented every 2 s. Each stimulus lasted one second and only one location was stimulated at a given time. The size of the stimulus varied depending on the visual protocol (see figure legends).

Because dCx responses adapt strongly to inter-stimulus interval (ISI) shorter than a few seconds, we typically set ISIs between 10 and 15 s (except in adapting protocols). Conversely, to ensure stationarity of brain state and recordings, we tried to keep stimulus-protocol durations to within 2-3 hours. These two constraints explain the relatively coarse resolution of the stimulation grid used in many experiments. Mapping RFs with sparse noise, 3×5 positions and 15-30 trials per position/contrast took about 2-4 hours.

In experiments with anesthetized animals, visual stimuli were presented on a flat screen and without compensatory stimulus warping. Therefore, although stimuli presented in different positions had the same size on the screen, they were not equal in visual angle: for example, a 10-cm square in the center of the screen (where the eye was centered) corresponded to $\sim 36^\circ$ of visual angle whereas the same 10-cm square presented in the periphery of the screen occupied $\sim 22^\circ$ of visual angle. Nevertheless, we chose to show receptive fields in terms of size on the screen, rather than compensating for this distortion after receptive field estimation.

Time-Frequency analysis of LFP and eCoG data

eCoG and LFP recordings were low-pass filtered (100 Hz cutoff) and re-sampled at 1 kHz. Stimulus-triggered time-frequency spectra were computed with a 512 ms-sliding window and averaged across trials. The visually-evoked power increase was quantified by normalization with the average power spectrum measured in a 500 ms-window preceding stimulus onset. For eCoG data, the peak frequency was measured from the normalized power spectrum computed for the channel with the largest power in the beta range (15 – 35 Hz), after averaging the time frequency spectrum across a 2 s-time window following flash onset. For LFP data recorded with depth electrodes, the peak frequency was measured from the time frequency spectrum averaged across all channels.

To compare response amplitude across stimulus category, eCoG responses measured on the channel with largest power in the beta range were reduced to a single scalar value by averaging the power between 15 and 35 Hz in the time-frequency plots, over a specific time window corresponding to 2.5 s post onset for flashed stimuli and 2 s to 12.5 s post onset for movie stimuli (therefore excluding the response evoked by the initial 2 s-flash of the first frame). The averaged power values were normalized to the power measured during spontaneous activity for each animal. We then used an n-factor ANOVA for unbalanced samples (anovan.m in MATLAB) and used a Tukey-Kramer multiple comparison correction (multcomp.m in MATLAB) to assess the significance ($p < 0.01$) of response amplitudes across stimulus categories.

Receptive field estimation

Spiking responses were convolved with a 250-ms Gaussian window and resampled in 50-ms time bins (100 ms for movie stimuli). For “sparse noise” and “movie stimuli”, receptive fields were estimated by computing the stimulus-triggered-average of the evoked spiking response relative to stimulus onset in each spatial position. For “test stimuli” in the adapting stimulation, receptive fields were estimated by stimulus-triggered averaging (because there was no spatial or temporal overlap between successive stimuli over the course of the estimated evoked response); for “adapting stimuli” (those presented at high rates so as to generate adaptation), we selected a subset of trials beforehand, so as to equalize averaged trial numbers between adapting and test stimuli. To estimate receptive fields in the “dense noise” condition, we considered the efficient stimulus to be the time derivative of the stimulus contrast: since dense-noise frames were displayed for several seconds (10 s), the change in stimulus contrast was a better predictor of the evoked response than the actual contrast. We then adopted a least-squares approach and solved the following equation for every 50-ms time bin following stimulus onset:

$$R(T+t) = \sum_{x,y} h_1(x,y,t) \times S(x,y,T) + \sum_{x,y} h_2(x,y,t) \times S^2(x,y,T), \quad \text{Equation 1}$$

where R is the spiking response; T , the time of stimulus onset; and h_1 and h_2 are the linear (first-order Volterra kernel) and nonlinear (diagonal of the second-order Volterra kernel) components of the RF at $t \times 50$ ms after stimulus onset (Emerson et al., 1987; Fournier et al., 2011). To improve the signal-to-noise ratio of the estimated RF components, we used a regularization method (ridge regression) to solve Equation 1. The optimal value of the regularization parameter was estimated by maximizing the percentage of explained variance using a 20-fold cross-validation procedure (Hastie et al., 2009; Machens et al., 2004).

The significance of the receptive field was measured using a jackknife analysis: we estimated 20 times the RF, each time omitting 5% of the data, and computed the standard error of the mean (SEM) from this collection of RF estimates. The mean receptive field was then converted to z-scores by normalization with the SEM. RFs were spatially interpolated for visualization. The spatial extent of the RF components was measured after spatial interpolation of the RF as the maximal area covered by responses that were 99%-significant (z-score > 2.33). Response latency of the neuron population was measured in each position at the first crossing of 50% of the maximum firing rate of the population receptive field in the first second following stimulus onset. The spatial modulation index was measured as the relative proportion of the energy of the RF that could not be explained by the spatial average response:

$$\text{Spatial modulation index} = \frac{\sum_{x,y,t} (h(x,y,t) - \langle h(x,y,t) \rangle_{x,y})^2}{\sum_{x,y,t} h(x,y,t)^2}. \quad \text{Equation 2}$$

For RFs estimated with sparse noise, the spatial modulation index was measured considering ON and OFF RFs as a single vector, i.e., by integrating over space, time and contrast in Equation 2.

The correlation coefficient between ON and OFF responses was measured as:

$$\text{ON} \times \text{OFF correlation} = \frac{\sum_{x,y,t} (h_{\text{ON}}(x,y,t) \times h_{\text{OFF}}(x,y,t))}{\sqrt{\sum_{x,y,t} (h_{\text{ON}}(x,y,t))^2 \times \sum_{x,y,t} (h_{\text{OFF}}(x,y,t))^2}}. \quad \text{Equation 3}$$

We quantified the correlation of a RF with the rest of the dCx population (Population correlation) as the Pearson's correlation coefficient between the RF of a given neuron (i) and the mean RF averaged across all other neurons recorded simultaneously ($j \neq i$):

$$\text{Population correlation } (i) = \frac{\sum_{x,y,t} (h^i(x,y,t) - \langle h^i \rangle_{x,y,t}) \times (\langle h^i(x,y,t) \rangle_{j \neq i} - \langle h^i \rangle_{x,y,t,j \neq i})}{\sqrt{\sum_{x,y,t} (h^i(x,y,t) - \langle h^i \rangle_{x,y,t})^2 \times \sum_{x,y,t} (\langle h^i(x,y,t) \rangle_{j \neq i} - \langle h^i \rangle_{x,y,t,j \neq i})^2}}. \quad \text{Equation 4}$$

The coefficient of spatial correlation of the RF was measured as the average correlation coefficient between the response of a neuron in a given position and the mean response of the same neuron averaged across all other positions.

$$\text{Spatial correlation} = \left\langle \frac{\sum_t (h(x,y,t) \times \langle h(x',y',t) \rangle_{x' \neq x, y' \neq y})}{\sqrt{\sum_t (h(x,y,t))^2 \times \sum_t (\langle h(x',y',t) \rangle_{x' \neq x, y' \neq y})^2}} \right\rangle_{x,y}. \quad \text{Equation 5}$$

For RFs estimated with dense noise, we defined the linearity index as the relative contribution of the linear RF component to the energy of the RF:

$$\text{Linearity index} = \frac{\sum_{x,y,t} h_1(x,y,t)^2}{\left(\sum_{x,y,t} h_1(x,y,t)^2 + \sum_{x,y,t} h_2(x,y,t)^2 \right)}. \quad \text{Equation 6}$$

The optimal spatial frequency of the linear RF component was measured as the peak of the 2D power spectrum at the time of maximal response. For neurons with non-zero preferred spatial frequency, we also measured the orientation of the linear receptive field component. Their orientation tuning curve was estimated at best spatial frequency by summing for each orientation the convolutions of the linear receptive field with two gratings in spatial quadrature (spatial phase of 0° and 90°). The estimated tuning curve was

fitted with a von Mises distribution M from which we measured the preferred orientation (Ori_{pref}) and the orientation selectivity index (OSI):

$$OSI = \frac{M(Ori_{pref})}{M(Ori_{pref}) + M(Ori_{pref} + 90^\circ)} \quad \text{Equation 7}$$

Bayesian decoding

To estimate the nature of the stimulus from the recorded spike trains, we used a Bayesian decoding approach, based on the standard formula:

$$P(s | n) = P(s) \times P(n | s), \quad \text{Equation 8}$$

where s is the stimulus variable and n the number of spikes. Assuming statistical independence of spikes recorded from N different cells and at different delays post stimulus onset (from 0 to T ms), we derived $P(n | s)$ as:

$$P(n | s) = \prod_{t=0,200,\dots,T} \prod_{i=1}^N P(n_{i,t} | s), \quad \text{Equation 9}$$

where $n_{i,t}$ corresponds to the number of spikes recorded from cell i in a 200 ms-time window t ms after stimulus onset.

The posterior probability of the stimulus being at a certain position given the recorded spike train was then computed as:

$$P(s | n) = CP(s) \times \prod_{t=0}^T \left[\left(\prod_{i=1}^N f_{i,t}(s)^{n_{i,t}} \right) \times \exp \left(-\tau \sum_{i=1}^N f_{i,t}(s) \right) \right], \quad \text{Equation 10}$$

where s is the stimulus variable representing the state of the stimulus (e.g., with #Xpos x #Ypos = 3×3 possible positions for movie stimuli); C is a normalization constant; $f_{i,t}$ is the stimulus triggered average response of cell i , t ms after stimulus onset and τ corresponds to the size of the spike count window (200 ms). Spike counts were measured for 2 s post-stimulus onset for sparse noise stimuli. For movie stimuli, spike counts were measured for 4 s post-stimulus onset when considering responses to movie onset and from 4 s post till the end of the movie when considering responses to movie presentation. The posterior probability and the stimulus-triggered average responses were computed on different sets of trials using a 20-fold cross-validation procedure, to avoid over-fitting.

In one experiment (turtle K5), three different movies were presented randomly during the same recording session. To decode both position and identity of the presented movie, we used the same approach as above except that both the position and the identity of the movie were decoded. Therefore, the stimulus variable s in Equation 10 had #Xpos x #Ypos x #movies = $3 \times 3 \times 3$ possible states.

For sparse noise, both stimulus position and contrast were decoded. In this case, the stimulus variable s in Equation 10 had #Xpos x #Ypos x #contrast = $3 \times 5 \times 2$ possible states.

The average posterior probabilities were computed by averaging $P(s | n)$ when the actual stimulus was in a particular state (position or position/contrast or position/movie identity).

This approach is similar to that previously used to reconstruct the position of an animal from place cell firing in hippocampal recordings (Bendor and Wilson, 2012; Zhang et al., 1998), except that we also considered the response time course as informative of the stimulus, by multiplying the probabilities obtained for different time delays after stimulus onset. The choice of the spike count bin size (200 ms) and the overall time window over which the response was considered were optimized to minimize the average decoding error (Figure S4F).

Peri-Oscillation Triggered Histograms and Current Source Density analysis

Beta-oscillations were extracted by filtering the LFP between 15 and 35 Hz. The peri-oscillation triggered histograms (POTH) were computed by trigger-averaging the spike count relative to the trough of the beta oscillation measured with a superficial electrode in the array (i.e., at the peak of the current sink) (Poo and Isaacson, 2009). The amplitude of each oscillation cycle was defined as the amplitude difference between peak and following trough; only cycles with an amplitude $\geq 4SD$ from the mean were used for computing the POTH. POTHs were normalized to the mean firing rate. For neurons that displayed a significant modulation of firing rate across beta oscillation cycles (Rayleigh test of non-uniformity, $p < 0.01$), we measured the preferred firing phase and the strength of the spike-LFP coupling from the position and the amplitude of the peak in the POTH.

Current-source-density (CSD) profiles were computed using the inverse current source density method (Pettersen et al., 2006), using a smoothing Gaussian kernel with a standard deviation = $2 \times$ electrode pitch.

QUANTIFICATION AND STATISTICAL ANALYSIS

Rayleigh test was utilized to test if a neuron had a significant modulation of its firing rate across phases of LFP beta oscillations. A n-factor ANOVA was used to measure the distance between eCoG responses to different stimulus categories; pairwise statistical

comparison between stimulus categories were then performed by using a Turkey-Kramer multiple comparison correction on the result of the ANOVA. Significance of receptive fields was measured by z-scoring the response with the SEM obtained using a jackknife analysis. The spatial extent of the receptive fields was measured as the maximal area covered by 99%-significant responses ($z\text{-score} > 2.33$). Correlation coefficients were measured to assess the selectivity of responses to movie frames across different positions. The Pearson's correlation was used to measure the correlation of receptive fields spatiotemporal profiles across the population of simultaneously recorded neurons. Student's t test for paired samples was used to compare properties of responses to movie onset and movie presentation; latencies of visual responses between rostral and caudal recording probes and spatial extent of ON and OFF receptive fields. Medians, means and standard deviations are reported throughout the text. Significance was defined at $p < 0.01$.

DATA AND SOFTWARE AVAILABILITY

Data and MATLAB code will be made available upon request.